



Functionally distinct subgroups of oligodendrocyte precursor cells integrate neural activity and execute myelin formation

Roberta Marisca^{1,2,6}, Tobias Hoche^{1,6}, Eneritz Agirre³, Laura Jane Hoodless¹, Wenke Barkey¹, Franziska Auer^{1,2}, Gonçalo Castelo-Branco^{3,4} and Tim Czopka^{1,2,5} ✉

Recent reports have revealed that oligodendrocyte precursor cells (OPCs) are heterogeneous. It remains unclear whether such heterogeneity reflects different subtypes of cells with distinct functions or instead reflects transiently acquired states of cells with the same function. By integrating lineage formation of individual OPC clones, single-cell transcriptomics, calcium imaging and neural activity manipulation, we show that OPCs in the zebrafish spinal cord can be divided into two functionally distinct groups. One subgroup forms elaborate networks of processes and exhibits a high degree of calcium signaling, but infrequently differentiates despite contact with permissive axons. Instead, these OPCs divide in an activity- and calcium-dependent manner to produce another subgroup, with higher process motility and less calcium signaling and that readily differentiates. Our data show that OPC subgroups are functionally diverse in their response to neurons and that activity regulates the proliferation of a subset of OPCs that is distinct from the cells that generate differentiated oligodendrocytes.

In the CNS of vertebrates, oligodendrocyte precursor cells (OPCs, also known as NG2 cells) comprise an abundant cell population that tiles the CNS throughout life¹. OPCs are the cellular source for new myelin during development, in response to neuronal activity in the context of myelin plasticity, and during regeneration of damaged myelin^{2–5}. We have a relatively robust understanding of the cell intrinsic signaling cascades and transcriptional changes that govern OPC differentiation into myelinating oligodendrocytes^{6,7}. However, there are more OPCs in the CNS than ever differentiate. Whether all OPCs equally contribute to myelin formation, or whether subsets of OPCs exist with different fates and functions, remains a major question.

Various attempts to compartmentalize OPC properties have revealed that these cells are indeed not a uniform population with equal properties^{8–13}. OPCs in different regions show different responsiveness to growth factors¹⁴ and vary in their capacity to differentiate when transplanted into other CNS areas¹⁵, and disease-specific OPC phenotypes have been identified in mouse models of multiple sclerosis and human multiple sclerosis patients^{16,17}. Furthermore, physiological properties of OPCs have been found to diversify increasingly over time¹⁸, and OPCs themselves can modulate neuronal firing¹⁹. Despite these findings, it remains unclear whether the reported diversity of OPC properties reflects subtypes of OPCs with distinct functions, either in the same or in different microenvironments; or whether it reflects different states of cells with the same function as they progress along their lineage. The reason for this is that it is inherently difficult to definitively monitor the dynamics of OPC lineage progression and function from single time point analyses, including those of sequencing datasets. So far, no study has carried out a systematic analysis of cell dynamics within

the oligodendrocyte lineage over time while probing the function and molecular states of OPC subsets in vivo. Such an analysis would help to advance our understanding of how oligodendrocyte lineage cells relate to each other. Specifically, it would reveal whether the different functions that are attributed to OPCs apply to all cells at a particular time point, or whether their lineage progression is less linear, with specializations of subgroups of OPCs that have distinct functions.

An analysis such as this would help to resolve open questions as to how neuronal activity affects OPC fates. OPCs integrate neuronal activity from surrounding axons by the expression of a wide range of neurotransmitter receptors and voltage-gated ion channels^{20–25}. However, the role of neural activity in regulating OPC fate decisions is still unclear because enhanced activity increases both proliferation and differentiation at the population level^{2,3,26–28}. This may be because subgroups of OPCs exhibit different electrophysiological properties and therefore differ in their sensitivity to axonal signals, or because they show differential cell fates in response to activity. In any case, the analysis of physiology, gene expression, or cell fate alone is not sufficient to reveal direct causality between heterogeneity in OPC properties and OPC fates.

Here, we address the diversity of OPC fates in an integrated approach by combining single-cell RNA sequencing in zebrafish, live-cell imaging of OPC properties and fates, calcium imaging, and manipulation of physiology to reveal how neural activity affects the ability of OPC subgroups to divide and differentiate.

Results

OPCs form a network composed of cells with distinct morphologies and dynamics. We generated transgenic zebrafish that spe-

¹Institute of Neuronal Cell Biology, Technical University of Munich, Munich, Germany. ²Graduate School of Systemic Neurosciences, Ludwig-Maximilian University of Munich, Planegg-Martinsried, Germany. ³Laboratory of Molecular Neurobiology, Department Medical Biochemistry and Biophysics, Biomedicum, Karolinska Institutet, Stockholm, Sweden. ⁴Ming Wai Lau Centre for Reparative Medicine, Stockholm Node, Karolinska Institutet, Stockholm, Sweden. ⁵Munich Cluster for Systems Neurology (SyNergy), Munich, Germany. ⁶These authors contributed equally: Roberta Marisca, Tobias Hoche. ✉e-mail: Tim.Czopka@tum.de

cifically label OPCs using *olig1* regulatory sequences (Fig. 1 and Supplementary Video 1)^{29,30}. Whole-animal and high-resolution imaging of OPC reporter animals showed that labeled cells form a network of cellular processes that extends throughout the CNS (Fig. 1a). Cross-sectional views at the level of the spinal cord revealed that OPC processes were found almost exclusively within the lateral spinal cord and much less frequently in the neuron-dense regions of the medial spinal cord (Fig. 1b). The regions of the lateral spinal cord contained myelinated and unmyelinated axons, as well as dendrites and synapses (Fig. 1c and Extended Data Fig. 1b,c). The OPC process network that intersperses these axo-dendritic areas persisted over the long term while OPC differentiation steadily increased, as shown by our analysis of OPC and myelinating oligodendrocyte numbers (Extended Data Fig. 1a,d,e).

To investigate how individual OPCs form this process network, we carried out OPC sparse labeling and three-dimensional morphometry of individual cells (Fig. 1d,g, Extended Data Fig. 1f,g and Supplementary Video 2). Our analysis revealed that OPC somata reside either within the neuron-rich areas of the medial spinal cord or within the axo-dendritic areas of the lateral spinal cord (Fig. 1e). Despite these different soma positions, the processes of each cell extended into axo-dendritic territories of the lateral spinal cord (Fig. 1e,f). Although the vast majority of all OPC processes could thus be found in the same local microenvironment, OPCs had distinct properties with regard to the size and dynamics of their processes, which correlated with the soma position of the respective cell. OPCs with their soma within neuron-rich areas of the medial spinal cord formed a much more elaborate process network than did OPCs that entirely resided within lateral axo-dendritic territories (Fig. 1g). Furthermore, OPCs showed very different process dynamics, depending on the position of the respective cell body. Time projections showed that OPCs in axo-dendritic areas almost completely remodeled their entire process network within 1 h, whereas OPCs that resided with somas in neuron-rich areas only remodeled their process tips while retaining stable major branches (Fig. 1h and Supplementary Videos 3–6). Together, these data show that OPCs in the zebrafish spinal cord segregate into two entities. The processes of all cells reside within the same local tissue, but branching complexity and process dynamics differ and correlate with the position of the respective cell body (Fig. 1i).

Single-cell RNA sequencing reveals distinct molecular signatures of OPCs. As we could distinguish OPCs with different properties relating to soma position, morphology and process dynamics, we

carried out transcriptome analysis of single OPCs using the Smart-Seq2 protocol (ref.³¹) to identify the molecular signatures that underlie the observed differences between OPCs (Fig. 2, Extended Data Fig. 2 and Supplementary Fig. 1). Clustering analysis of 310 cells that were isolated from OPC reporter animals at 5 d post fertilization (d.p.f.) led to the identification of five clusters (#1–#5) with oligodendrocyte lineage identity, based on the co-expression of the key lineage transcription factor genes *sox10*, *nkx2.2a*, and *olig2* (Fig. 2a,b and Extended Data Fig. 2c,d). We confirmed oligodendrocyte lineage identity of cells labeled in our transgenic lines by in situ hybridization and immunohistochemistry, and found that almost all OPCs detected by the transgene co-expressed *sox10* and *nkx2.2a* (Fig. 2c and Extended Data Fig. 2c). Two additional clusters (#6 and #7) were negative for oligodendrocyte lineage markers and therefore not investigated further (Supplementary Fig. 1a and Extended Data Fig. 2c–e). Among the five oligodendrocyte clusters, clusters #1 to #4 expressed markers for OPCs, such as *ppp1r14bb*, and no markers of mature differentiated oligodendrocytes, like *plp1a* and *mpba*, which were only present in cluster #5 (Fig. 2b and Extended Data Fig. 2e). Therefore, clusters #1 to #4 probably represent the OPCs investigated in our imaging studies.

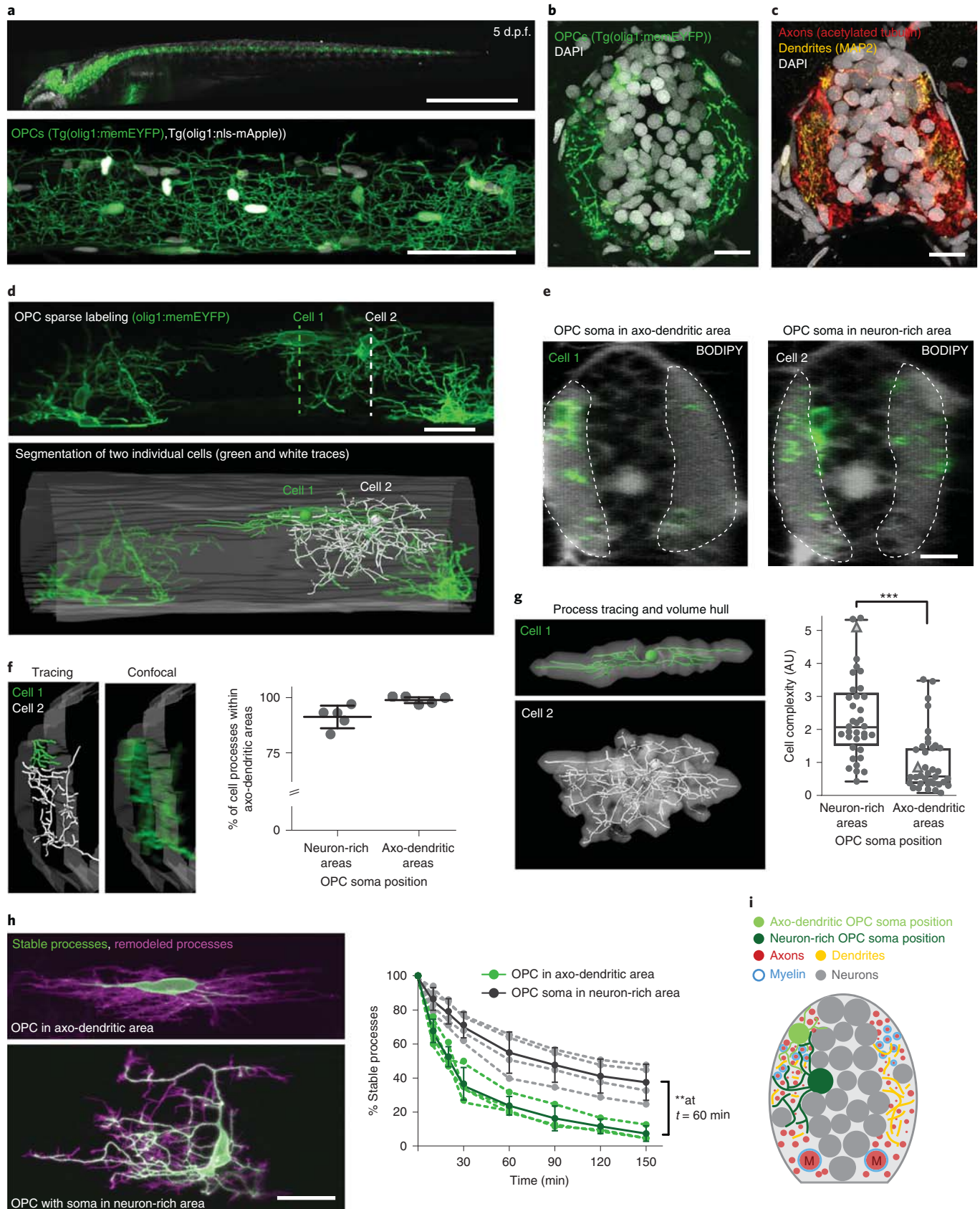
To determine how the OPC clusters identified by transcriptomic analysis correlate with the cells seen by live-cell imaging, we carried out in situ hybridizations of genes that were differentially expressed between clusters and determined the position of the respective OPC soma. The bona fide OPC marker *cspg4* was enriched in clusters #1, #2 and #3 (Fig. 2d,e). In situ, 82% of OPC somata (*olig1:nls-mApple*-positive, *mbp:nls-EGFP*-negative) in neuron-rich areas of the medial spinal cord were *cspg4*-positive, and only about one third of OPCs in axo-dendritic areas (Fig. 2e and Extended Data Fig. 2f). Another OPC marker, *ptprz1b*, which predominantly clustered to OPC #1 and #2, was also expressed by more OPCs in neuron-rich areas than in axo-dendritic areas (Fig. 2d,f). Clusters #2 and #3 expressed the OPC marker *cspg4* but also expressed cell cycle genes. Here, cluster #2 contained genes specific for S phase, like *pcna*, whereas cluster #3 was enriched for genes specific for M phase, like *mki67* (Fig. 2g,h and Supplementary Fig. 1e,f). To determine where proliferative OPCs predominantly localize, we assessed the incorporation of the thymidine analogue 5-ethynyl-2'-deoxyuridine (EDU) and found comparable numbers of dividing OPCs in the medial and lateral spinal cord (Fig. 2i and Extended Data Fig. 2f).

In contrast to clusters #1–#3, cluster #4 expressed only low levels of *cspg4* messenger RNA, but high levels of *gpr17*, which is a marker for a subset of OPCs and early differentiating

Fig. 1 | Characteristics of OPCs in zebrafish. **a**, Top: image of whole Tg(*olig1:memEYFP*) transgenic animal at 5 d.p.f. Scale bar, 1 mm. Bottom: confocal image of a Tg(*olig1:memEYFP*),Tg(*olig1:nls-mApple*) zebrafish at the level of the spinal cord at 5 d.p.f. Scale bar, 50 μ m. Representative images from four animals in two independent experiments. **b**, Cross-sectional view of the spinal cord showing the distribution of OPC processes in Tg(*olig1:memEYFP*) at 7 d.p.f.; $n = 33$ animals in 11 experiments. Scale bar, 10 μ m. **c**, Cross-sectional view of the spinal cord showing the distribution of axons and dendrites at 7 d.p.f., visualized with anti-acetylated tubulin and anti-MAP2; $n = 7$ animals in two experiments. Scale bar, 10 μ m. **d**, Top: sparse labeling of *olig1:memEYFP*-expressing OPCs at 4 d.p.f. Bottom: tracing of two neighboring exemplary OPCs and the spinal cord outlines. n values are given in **g**. Dotted lines indicate the position of the y -axis rotations shown in **e**. **e**, 90° y -axis rotations at the level of the soma of the two cells shown in **d** with a BODIPY counterstain to reveal the position of OPC somata in axo-dendritic (cell #1) and neuron-rich (cell #2) regions. $n = 12$ BODIPY stained animals in four experiments. Dotted lines indicate axo-dendritic areas. Scale bar, 10 μ m. **f**, High-magnification view showing the proximity of the processes made by the two OPCs in **d** within axo-dendritic areas. Quantification shows the percentage of cell processes resident in axo-dendritic areas formed by OPCs with their soma in neuron-rich and axo-dendritic regions at 4–5 d.p.f. ($91.3\% \pm 2.3$ s.d. neuron-rich versus $98.9\% \pm 0.7$ s.d. axo-dendritic). $n = 5$ cells per condition from six animals. **g**, Morphology reconstructions of the two OPCs shown in **d–f**. Quantification shows relative cell complexities of individual OPCs with their soma in different areas at 4 d.p.f. Triangles indicate example cells #1 and #2. Boxes represent the median (center line) and the 25th and 75th percentiles ($2.1 \pm 1.5/3.2$ for OPCs in neuron-rich areas versus $0.6 \pm 0.4/1.5$ in axo-dendritic areas), and whiskers indicate the minimum and maximum values. $P < 0.001$, Mann-Whitney U test, $U = 211$, $n = 36$ and $n = 38$ cells, respectively, from 23 animals in 11 experiments. **h**, Projections of 60 min time-lapse imaging show remodeled and stable processes of OPCs with their soma in different areas. Quantification shows stable processes over time. Dashed lines connect data points of individual cells. Data points connected by continuous lines represent mean \pm s.d. within the groups. At $t = 60$ min: $56.3 \pm 12.2\%$ stable processes for OPCs in neuron-rich areas versus $25.0 \pm 5.5\%$ in axo-dendritic areas. $P = 0.001$ between groups, two-way repeated measures ANOVA of 0–60 min time points, $F(1,6) = 32$, $n = 4$ cells per group from eight animals in eight experiments. Scale bar, 20 μ m. **i**, Schematic overview depicting the position of OPCs in the zebrafish spinal cord.

oligodendrocytes in mammals (Fig. 2j)^{32,33}. Furthermore, cluster #4 contained genes associated with oligodendrocyte differentiation, such as *myrf*, suggesting a committed oligodendrocyte pre-

cursor identity (Fig. 2j)^{10,34}. However, these cells still expressed proliferation-related genes (Fig. 2g and Supplementary Fig. 1e,f), meaning that they were not post-mitotic differentiating oligo-



dendrocytes. In situ hybridization showed that *gpr17* and *myrf* predominantly labeled OPCs within axo-dendritic areas (Fig. 2k,l and Extended Data Fig. 2f). In line with our marker analysis, gene ontology (GO) term analysis of genes enriched in cluster #4 contained genes involved in early differentiation, as well as proliferation genes (Fig. 2m and Supplementary Table 1). By contrast, OPC cluster #1 contained terms related to neurotransmitter sensing but lacked markers associated with differentiation (Fig. 2n and Supplementary Table 1).

In summary, our data show that proliferative OPCs (clusters #2–#4) were present in both regions of the spinal cord. Quiescent OPCs characteristic of cluster #1 were found predominantly in neuron-rich areas of the medial spinal cord, where OPCs are characterized by an elaborate process network with slow process dynamics. OPCs with genes indicative of differentiation and proliferation in cluster #4 were predominantly found within axo-dendritic areas of the lateral spinal cord, where cells with a simpler process network and rapid remodeling dynamics reside. Therefore, our data indicate that OPCs with their soma in axo-dendritic and neuron-rich areas have different capacities to integrate signals from axons and to differentiate towards myelinating oligodendrocytes.

Fates of OPC subpopulations. Having identified OPCs with distinct characteristics and soma positions, which correlated with different molecular profiles of OPC sequencing clusters, we wanted to confirm their differentiation fates using time-lapse imaging. As predicted from our sequencing data, OPC divisions occurred in all areas of the spinal cord (Fig. 3a). However, within 24 h of investigation, the vast majority of OPCs within axo-dendritic areas began to differentiate and to ensheath axons, whereas none of the OPCs with their soma in the neuron-rich areas did so during the same time frame (Fig. 3a and Supplementary Videos 7,8). To exclude the possibility that OPCs located in the neuron-rich areas would simply differentiate at later stages, we carried out long-term analysis of individual OPCs until 14 d.p.f. A retrospective inspection of 95 differentiated oligodendrocytes identified by the formation of myelin sheaths showed that, independent of animal age, the vast majority of differentiated OPCs resided within axo-dendritic areas (Fig. 3b). Most of these later differentiating cells also showed the characteristic morphology of fast remodeling OPCs with low process complexity (Extended Data Fig. 3). Population analysis further confirmed that the relative proportion of myelinating cells with their soma in neuron-rich areas always remained a minority of no more than 11% of all myelinating oligodendrocytes throughout the analysis period (Fig. 3c). It is important to note that all OPC processes extend into the same axo-dendritic territories, regardless of the position of the respective cell body (Fig. 1f). Therefore, all OPCs can contact

myelination-competent axons, especially because a single OPC can span the entire dorso-ventral and medio-lateral dimensions of the spinal cord (Extended Data Fig. 1f,g). Indeed, triple labeling of individual axons and OPCs in a transgenic line in which all myelin was labeled showed that a single OPC could persist undifferentiated over long time periods while its processes were in close proximity to an axon that became increasingly myelinated during the same time (Fig. 3d). Therefore, these data show that OPCs that reside with their soma in neuron-rich areas can remain undifferentiated despite extending their processes into areas with axons that are permissive for myelination.

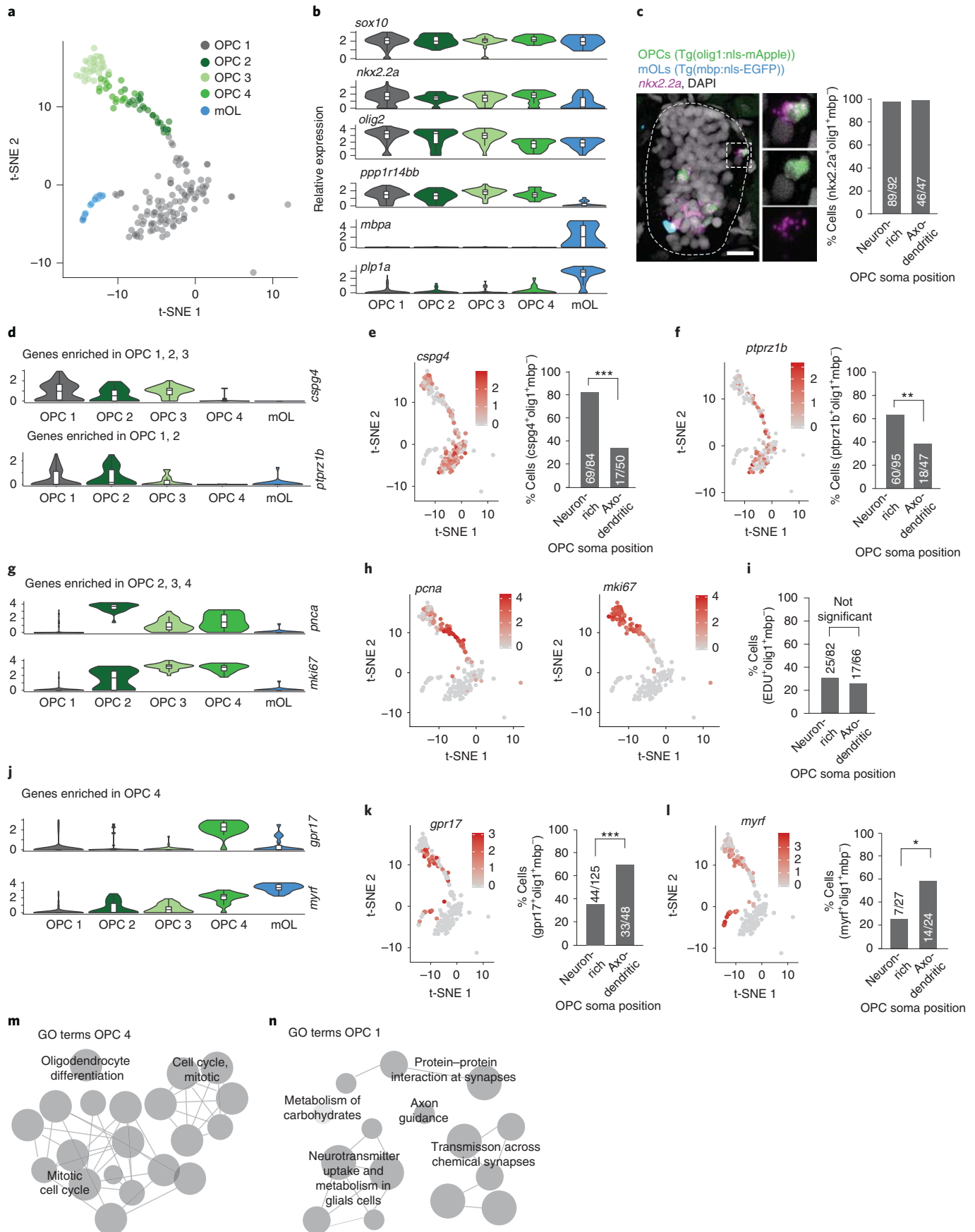
Interrelationships between OPC subpopulations. The finding that one subset of OPCs frequently differentiates while another rarely does so raised the question of how these two populations relate to one another. Where do readily differentiating OPCs within axo-dendritic areas come from? One possibility is that slow remodeling, high-complexity OPCs migrate into axo-dendritic areas where they acquire the phenotype of the fast remodeling OPCs that are typically found within these regions. In such a case, the same OPC would switch phenotype (Fig. 4a). Alternatively, new OPCs could arise in axo-dendritic areas from cell divisions of OPCs with their soma in neuron-rich areas, in which case one or two new cells with a different phenotype would emerge (Fig. 4a).

To address these two possible scenarios, we used time-lapse analysis of transgenic animals that expressed fluorescent reporters targeted to the nucleus of each OPC (Extended Data Fig. 4 and Supplementary Video 9). The nuclear label enabled us to trace the entire OPC population within tissue volumes and to simultaneously determine OPC phenotype based on the simple observation that the shape of the OPC nucleus appeared round when located in neuron-rich areas and elongated when located in axo-dendritic areas of the lateral spinal cord (Fig. 4b). Proliferative OPCs were present in both neuron-rich and axo-dendritic areas, and they divided with similar cell cycle times, further confirming their precursor state (Fig. 4c,d). During the time of analysis, 70% of OPCs with their soma in neuron-rich areas retained their position (Fig. 4e and Extended Data Fig. 4b), whereas 27% divided and one or both daughter cells subsequently emerged in axo-dendritic areas (Fig. 4c,e). For only 3% of OPCs, we observed direct soma migration from neuron-rich to axo-dendritic areas that we could not link to a cell division (Fig. 4e). Likewise, in a retrospective analysis of the origin of OPCs in axo-dendritic areas, we found that 52% of cells arose from divisions of OPCs in neuron-rich areas, and 44% arose from OPC divisions in axo-dendritic areas (Fig. 4c,f). Direct, proliferation-independent migration of the same OPC was only observed in three cases (Fig. 4e,f). These

Fig. 2 | Single-cell RNA sequencing of zebrafish OPCs. **a**, t-SNE plots of olig1:memEYFP-sorted cells with oligodendrocyte lineage identity. There were 110, 28, 33, 18 and 19 cells in clusters 1–5, respectively. Cells derived from 2,300 animals at 5 d.p.f. (one experiment). **b**, Log(TPM) expression levels of key oligodendrocyte lineage markers in the clusters shown in **a**. Data are expressed as medians with interquartile ranges and a violin shape to represent the data distribution. **c**, In situ hybridization for *nkx2.2a* on transverse spinal cord sections of 7 d.p.f. Tg(olig1:nls-mApple),Tg(mbp:nls-EGFP) animals and quantification of *nkx2.2a*-expressing OPCs (olig1:nls-mApple-positive, mbp:nls-EGFP-negative) in neuron-rich and axo-dendritic areas (97% (89/92) versus 98% (46/47) positive cells). $n=12$ animals in three experiments. Dotted lines in the image indicate the outlines of the spinal cord. Scale bar, 10 μm . **d**, Violin plots with relative expression levels of *cspg4* and *ptrz1b*. **e**, t-SNE plots (n values shown in **a**) of *cspg4* expression and quantification of *cspg4*-positive cells as described in **c** (82% (69/84) versus 34% (17/50) positive cells). $P < 0.001$, two-tailed Fisher's exact test, $n=15$ animals in four experiments. **f**, t-SNE plots as in **e** of *ptrz1b* expression and quantification of *ptrz1b*-positive cells as described in **c** (63% (60/95) versus 38% (18/47) positive cells). $P=0.007$, two-tailed Fisher's exact test, $n=6$ animals in two experiments. **g**, Violin plots as in **b** with relative expression levels of *pcna* and *mki67*. **h**, t-SNE plots as in **e** of *pcna* and *mki67* expression. **i**, Quantification of proliferative OPCs using EDU incorporation (olig1:nls-mApple-positive, mbp:nls-EGFP-negative) in neuron-rich and axo-dendritic areas (30% (25/82) versus 26% (17/66) positive cells). $P=0.585$, two-tailed Fisher's exact test, $n=3$ animals in two experiments. **j**, Violin plots as in **b** with relative expression levels of *gpr17* and *myrf*. **k**, t-SNE plots as in **e** of *gpr17* expression and quantification of *gpr17*-positive cells as described in **c** (35% (44/125) versus 69% (33/48) positive cells). $P < 0.001$, two-tailed Fisher's exact test, $n=13$ animals in three experiments. **l**, t-SNE plots as in **e** of *myrf* expression and quantification of *myrf*-positive cells as described in **c** (26% (7/27) versus 58% (14/24) positive cells). $P=0.025$, two-tailed Fisher's exact test, $n=6$ animals in two experiments. **m**, GO terms of top 30 significantly expressed genes in cluster OPC #4. **n**, GO terms of top 30 significantly expressed genes in cluster OPC #1.

data indicate that OPCs do not switch states by changing their soma position; instead, this process is tightly linked to cell divisions and thus to the formation of a new cell.

Long-term contribution to myelination by OPCs in neuron-rich areas. To investigate how OPCs in neuron-rich areas contribute to the generation of myelinating oligodendrocytes, we followed their



fates over several days beginning at different time points between 3 and 21 d.p.f. (Fig. 5a, Extended Data Fig. 5 and Supplementary Fig. 2). Among all cells analyzed, 73% of the starting population divided, while the rest remained quiescent (Fig. 5b). None of the non-dividing cells differentiated to myelinating oligodendrocytes (Fig. 5b). However, we did observe the formation of new myelinating oligodendrocytes from daughter cells in 52% of the dividing OPCs (Fig. 5b). Ninety-two per cent of myelinating oligodendrocytes that formed from the starting population differentiated within 3 d after a cell division (Fig. 5c). Most of these newly formed myelinating cells localized within axo-dendritic areas, where they appeared within 1 d after the cell division (Fig. 5d). Interestingly, about 18% of oligodendrocytes differentiated while retaining their soma in neuron-rich areas, and these differentiation events also occurred within 3 d after a cell division (Fig. 5c). To test the importance of a recent cell cycle to the formation of new OPCs that are more competent to differentiate, we experimentally enhanced oligodendrocyte differentiation using the previously described silent information regulator 2 protein (Sir2p) inhibitor splitomicin³⁵, which enhanced myelinating oligodendrocyte numbers by 50% (Fig. 5e). Cell fate analysis of individual OPCs with their soma in neuron-rich areas over three consecutive days showed that myelinating oligodendrocytes arose from dividing OPCs in all cases (Fig. 5f). None of the quiescent, non-proliferative OPCs gave rise directly to myelinating oligodendrocytes, with or without splitomicin (Fig. 5f).

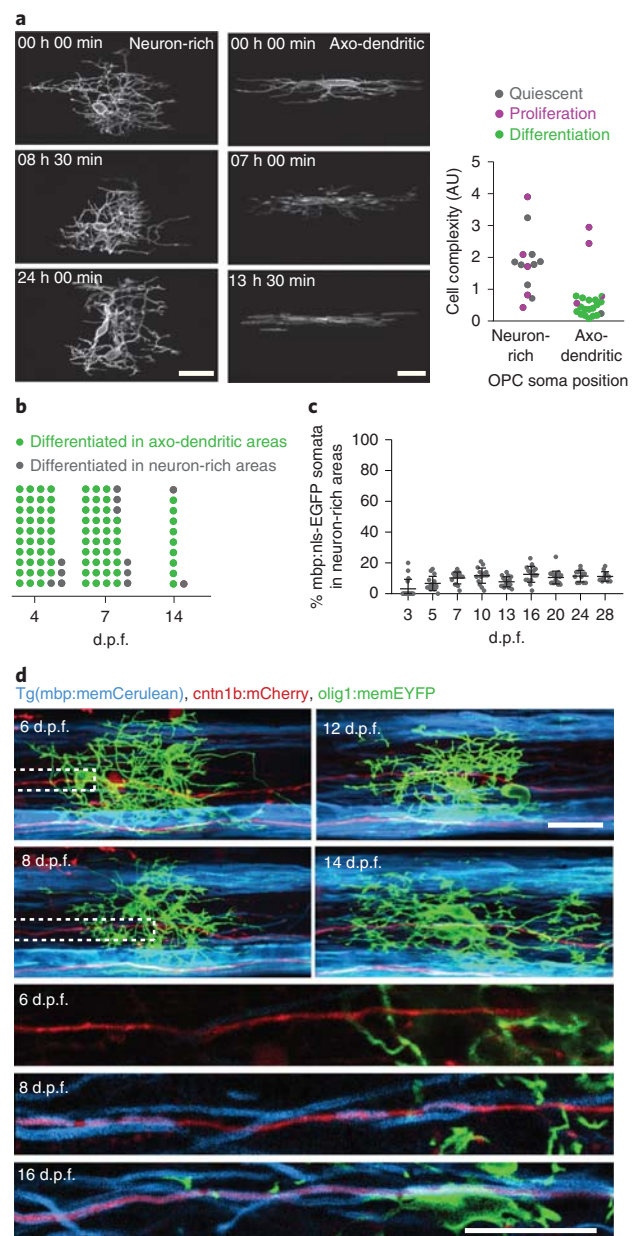
From these cell fate analyses, we conclude that a hierarchy between the two OPC subgroups exists. OPCs with high process complexity and slow remodeling dynamics located with their soma in neuron-rich areas probably do not differentiate directly, but they can divide to produce daughter cells with higher cell motility and a higher likelihood of differentiating into myelinating oligodendrocytes (Fig. 5g).

OPC subgroups show different degrees of calcium signaling activity. Because the infrequently differentiating OPCs (cluster #1) with their soma in neuron-rich areas were strongly enriched in genes important for neurotransmitter signaling, we asked whether

these cells communicate with axons in a manner distinct from that of OPCs in axo-dendritic areas that are more likely to myelinate. In such a scenario, rarely differentiating OPCs with high process complexity and slow remodeling dynamics might act as a cohort of cells with sensory functions to integrate signals from neurons. To assess this possibility, we expressed the genetically encoded calcium indicator GCaMP6m in OPCs, as OPCs have previously been shown to respond to neural activity with intracellular calcium increases^{22,36–38} (Fig. 6). Fast (10 Hz) imaging showed that GCaMP transients in OPCs lasted several seconds on average (Fig. 6b). Using membrane associated GCaMP6m-CAAX, we detected two different types of GCaMP transients (Fig. 6c–f and Supplementary Videos 10,11). Most OPCs showed transients that were restricted to process subdomains (Fig. 6c,d,f and Supplementary Video 10). In some cases, however, GCaMP transients spread throughout the entire cell (Fig. 6e,f and Supplementary Video 11). We also noticed that neighboring OPCs did not necessarily show the same transients during the recording (Fig. 6c,e). To investigate whether subgroups of OPCs show differential calcium signaling activity, we carried out population

Fig. 3 | Differentiation properties of individual OPCs. **a**, Example time-lapses of individually labeled olig1:memEYFP cells with their soma in neuron-rich (left) and axo-dendritic (right) spinal cord between 3 and 5 d.p.f. Quantification shows proliferation-differentiation fate within 24 h; 38% (5/13) versus 19% (4/21) cells proliferated and 0% (0/13) versus 81% (17/21) cells differentiated in neuron-rich versus axo-dendritic areas. $P = 0.254$ and $P < 0.001$, two-tailed Fisher's exact test, $n = 11$ animals in eight experiments. Scale bar, 20 μm . **b**, Frequency distribution of OPC soma position before differentiation at different developmental stages. Percentages of cells in axo-dendritic areas were 90.7% (39/43) at 4 d.p.f., 86.0% (37/43) at 7 d.p.f. and 81.8% (9/11) at 14 d.p.f.; $n = 18$, $n = 16$ and $n = 4$ animals in three, six and three experiments, respectively. **c**, Myelinating oligodendrocyte numbers with their soma in neuron-rich areas at different developmental stages. Data are expressed as mean percentage \pm s.d. Percentages were 3.1 ± 6.2 at 3 d.p.f. ($n = 17$ animals in two experiments), 6.7 ± 4.7 at 5 d.p.f. ($n = 15$ animals in three experiments), 10.3 ± 3.9 at 7 d.p.f. ($n = 15$ animals in three experiments), 11.8 ± 5.0 at 10 d.p.f. ($n = 16$ animals in three experiments), 12.7 ± 5.2 at 16 d.p.f. ($n = 17$ animals in two experiments), 10.6 ± 4.2 at 20 d.p.f. ($n = 20$ animals in three experiments), 11.5 ± 3.8 at 24 d.p.f. ($n = 12$ animals in three experiments) and 11.3 ± 3.1 at 28 d.p.f. ($n = 13$ animals in three experiments). **d**, Example images of an individual OPC with its soma in neuron-rich areas between 6 and 16 d.p.f., while a cntn1b:mCherry-labeled axon in close proximity becomes ensheathed with mbp:memCerulean-labeled myelin (observation from one animal). Dotted boxes indicate the position of magnified views (bottom three panels). Scale bar, 20 μm .

a, Example time-lapses of individually labeled olig1:memEYFP cells with their soma in neuron-rich (left) and axo-dendritic (right) spinal cord between 3 and 5 d.p.f. Quantification shows proliferation-differentiation fate within 24 h; 38% (5/13) versus 19% (4/21) cells proliferated and 0% (0/13) versus 81% (17/21) cells differentiated in neuron-rich versus axo-dendritic areas. $P = 0.254$ and $P < 0.001$, two-tailed Fisher's exact test, $n = 11$ animals in eight experiments. Scale bar, 20 μm . **b**, Frequency distribution of OPC soma position before differentiation at different developmental stages. Percentages of cells in axo-dendritic areas were 90.7% (39/43) at 4 d.p.f., 86.0% (37/43) at 7 d.p.f. and 81.8% (9/11) at 14 d.p.f.; $n = 18$, $n = 16$ and $n = 4$ animals in three, six and three experiments, respectively. **c**, Myelinating oligodendrocyte numbers with their soma in neuron-rich areas at different developmental stages. Data are expressed as mean percentage \pm s.d. Percentages were 3.1 ± 6.2 at 3 d.p.f. ($n = 17$ animals in two experiments), 6.7 ± 4.7 at 5 d.p.f. ($n = 15$ animals in three experiments), 10.3 ± 3.9 at 7 d.p.f. ($n = 15$ animals in three experiments), 11.8 ± 5.0 at 10 d.p.f. ($n = 16$ animals in three experiments), 12.7 ± 5.2 at 16 d.p.f. ($n = 17$ animals in two experiments), 10.6 ± 4.2 at 20 d.p.f. ($n = 20$ animals in three experiments), 11.5 ± 3.8 at 24 d.p.f. ($n = 12$ animals in three experiments) and 11.3 ± 3.1 at 28 d.p.f. ($n = 13$ animals in three experiments). **d**, Example images of an individual OPC with its soma in neuron-rich areas between 6 and 16 d.p.f., while a cntn1b:mCherry-labeled axon in close proximity becomes ensheathed with mbp:memCerulean-labeled myelin (observation from one animal). Dotted boxes indicate the position of magnified views (bottom three panels). Scale bar, 20 μm .



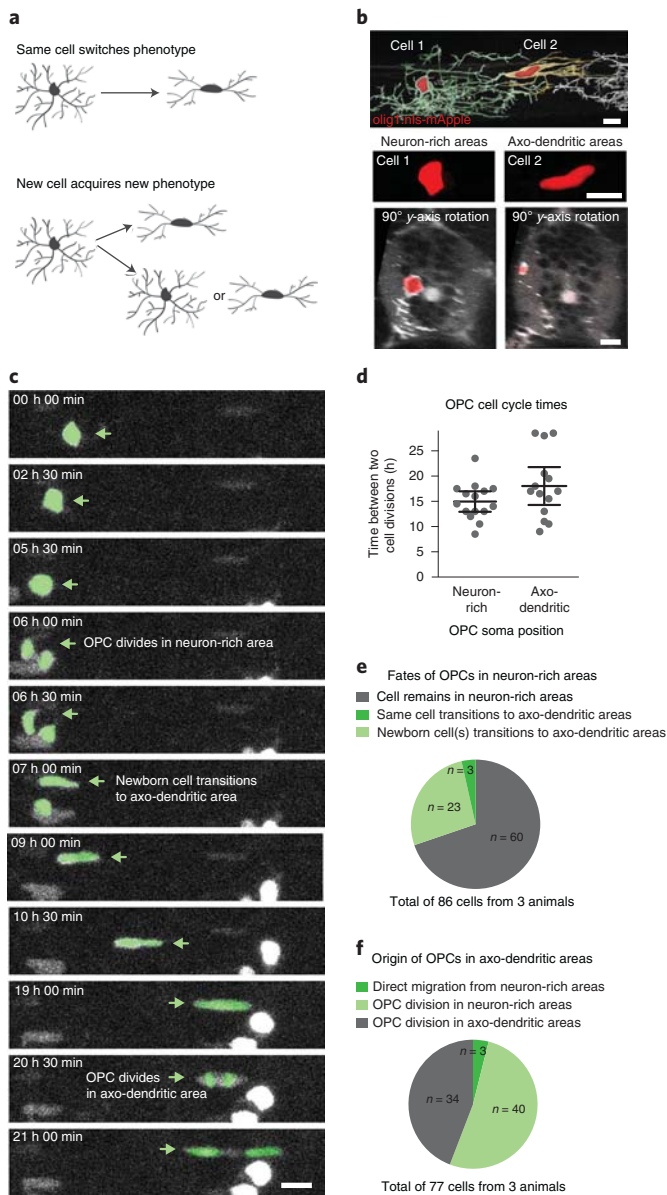


Fig. 4 | Interrelationships between OPC populations. **a**, Schematic overview delineating possible scenarios of OPC interrelations. **b**, Example image of two neighboring OPCs showing that OPCs with their soma in neuron-rich (cell #1) and axo-dendritic areas (cell #2) can be distinguished by the shape of their cell body. $n > 10$ animals in more than three experiments. Scale bar, 10 μm . **c**, Selection of time-lapse images over 21 h acquired at 30 min intervals in $\text{Tg}(\text{mbp}:\text{nls-EGFP}), \text{Tg}(\text{olig1}:\text{nls-mApple})$ zebrafish at 3 d.p.f. showing an OPC division in neuron-rich areas that gives rise to a daughter OPC in axo-dendritic areas, followed by another cell division. $n = 3$ animals in two experiments. Scale bar, 10 μm . **d**, Times between two cell divisions of OPCs, with their soma in neuron-rich and axo-dendritic areas as shown in **c**. Data are expressed as mean \pm 95% confidence interval (15.0 ± 0.9 h versus 18.0 ± 1.7 h). $n = 15$ and $n = 14$ cells from three animals in two experiments. **e**, Quantification of the fates of OPCs found in neuron-rich areas as shown in **c**. $n = 86$ cells from three animals in two experiments. **f**, Quantification of the origin of OPCs found in axo-dendritic areas as shown in **c**. $n = 77$ cells from three animals in two experiments.

analysis of somatic calcium increases in spinal cord volumes of full transgenic OPC GCaMP reporter animals (Fig. 6g, Extended Data Fig. 6 and Supplementary Video 12). Somatic GCaMP transients

could remain restricted to single OPCs (Fig. 6g), affect groups of cells, or even affect all cells (Extended Data Fig. 6d). However, in all animals investigated, OPCs within axo-dendritic areas had a 30% lower probability of showing GCaMP transients than did OPCs that extended their processes into axon-dendritic areas but resided with their soma in the medial spinal cord (Fig. 6h). Furthermore, the amplitudes of somatic GCaMP transients were significantly lower in OPCs within axo-dendritic areas than in OPCs with their soma in the medial spinal cord (Fig. 6i). In conclusion, the OPC subgroup that is less likely to differentiate directly, but which can divide to produce myelinating daughter cells, shows higher rates of calcium signaling activity.

Manipulation of neural activity and OPC calcium signaling primarily affects proliferation. If the subgroup of non-myelinating OPCs in neuron-rich areas is more responsive to axonal firing, as suggested by our GCaMP imaging data, the question arises as to how manipulation of neuronal activity affects the proliferation and differentiation behavior of OPC subgroups. We enhanced neural activity using bath application of the voltage-gated potassium channel blocker 4-aminopyridine (4-AP) (Fig. 7a). Single-plane confocal imaging of OPC GCaMP6m transients revealed that acute application of 0.5 mM 4-AP enhanced the frequency of GCaMP increases in OPC processes within 15 min, which was partially reversible by subsequent incubation with the voltage-gated sodium channel blocker tetrodotoxin (TTX) (Fig. 7b). These manipulations suggest that a proportion of the increased OPC GCaMP transients induced by 4-AP are mediated by alterations in neuronal activity.

To investigate how changes in neural activity and OPC calcium signaling affect cell behavior, we developed a protocol for chronic 4-AP treatment, which enhanced swimming behavior and GCaMP activity in neurons without inducing detectable deleterious effects on tissue integrity or inflammation as assessed by macrophage recruitment (Extended Data Fig. 7a–c). Six hours of 4-AP incubation resulted in a significant increase in EDU incorporation, which was blocked in the presence of TTX (Fig. 7c). This increase in EDU-positive OPCs was caused mainly by cells that reside in neuron-rich areas, whereas the number of EDU-positive OPCs within axo-dendritic areas remained unaltered (Fig. 7d). We also detected a small increase in the number of myelinating oligodendrocytes after 2 d of 4-AP incubation, which was, however, much less pronounced (Fig. 7e and Extended Data Fig. 7d).

Finally, we tested whether intracellular calcium signaling is necessary for 4-AP triggered proliferation by expressing the calcium exporting pump hPMCA2w/b (referred to as CalEx) in order to reduce OPC calcium signaling, as was recently demonstrated in astrocytes³⁹. Single OPCs that expressed mCherry-CalEx showed division rates similar to those of control cells (Fig. 7f,g). However, in contrast to control OPCs, in which 4-AP application triggered cell divisions (Fig. 7f), OPCs that expressed mCherry-CalEx did not show increased proliferation upon 4-AP incubation (Fig. 7g). Therefore, these data indicate that neural activity differentially affects the proliferation of distinct OPC subgroups, and that the OPC divisions triggered by 4-AP application require intracellular calcium signaling.

Discussion

Various differences have been assigned to OPC subsets, depending on origin, age, and local environment in the healthy and diseased brain^{8,40}. A major remaining question is to what extent the observed differences represent subtypes of OPCs with different functions versus different states of cells that have the same function. Our results reveal that the zebrafish spinal cord consists of OPC subtypes with distinct functions related to regulation of OPC numbers and to differentiation into myelinating oligodendrocytes. Such specializations may either be intrinsically determined or be induced by

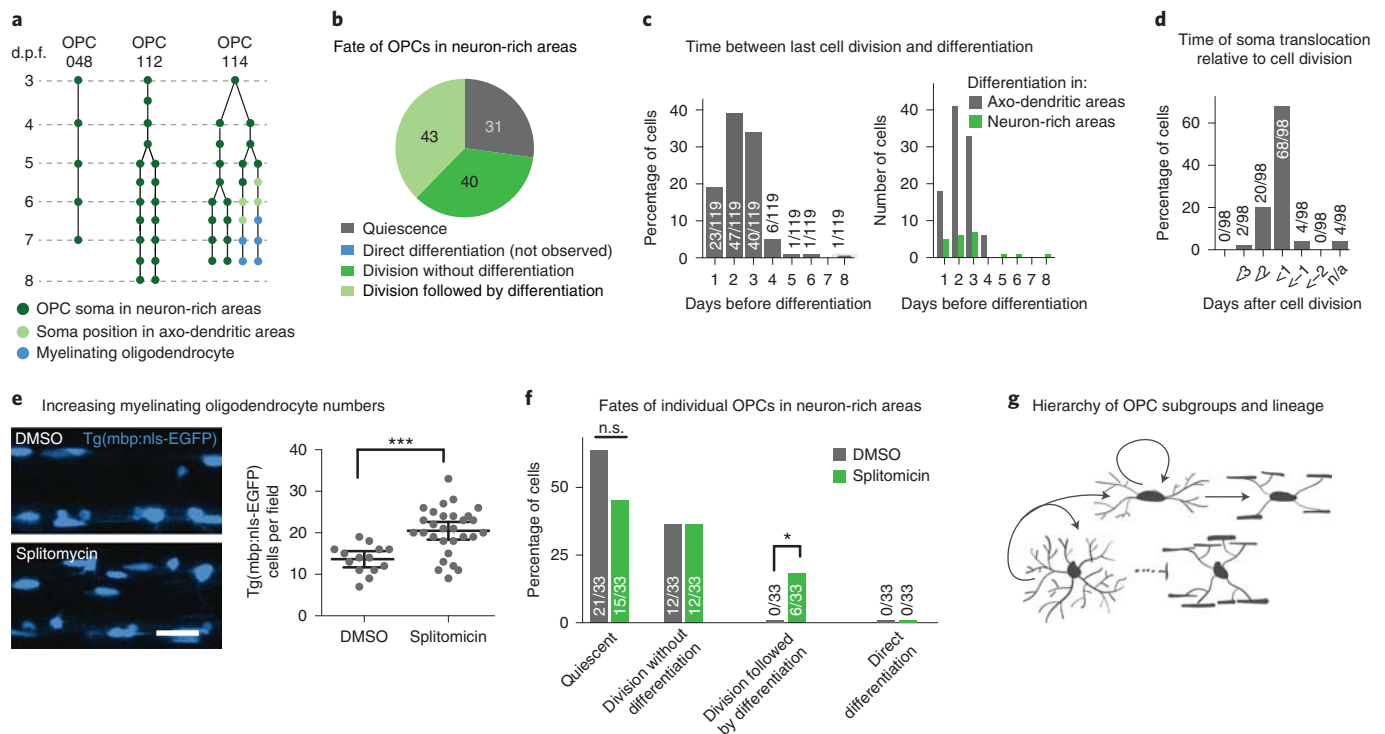


Fig. 5 | Long-term contribution to myelinating oligodendrocytes through proliferation-mediated generation of new OPCs. **a**, Example trees of OPC fates for cells with their cell body in neuron-rich areas. $n = 114$ starting cells from 45 fish in nine experiments between 3 and 26 d.p.f. These expanded to 270 cells, 119 of which differentiated. See also Extended Data Fig. 5b and Supplementary Fig. 2. **b**, Frequency distribution of proliferation and differentiation events observed in individual OPCs in neuron-rich areas over at least 4 d, unless all cells of the clone differentiated earlier. $n = 114$ cells; see **a**. **c**, Quantification of the time between last cell division before OPC differentiation and differentiation, expressed as a percentage of all cells analyzed (left) and as absolute numbers for cells with their cell body in neuron-rich and axo-dendritic areas (right) $n = 119$ cells; see **a**. **d**, Quantification of the timing of cell body translocation from neuron-rich to axon-rich areas relative to cell division. $n = 98$ cells; see **a**. **e**, Representative images and quantification of increased oligodendrocyte differentiation at 4 d.p.f. after splitomicin treatment. Data shown as mean \pm 95% confidence interval (13.6 ± 0.9 cells per field versus 20.4 ± 1.0 cells per field). $P < 0.001$, two-tailed unpaired t -test, $t = 4.184$, d.f. = 41, $n = 14$ and $n = 29$ animals in four experiments. Scale bar, 20 μ m. **f**, Fates of OPCs in neuron-rich areas between 3 and 5 d.p.f. in the presence and absence of splitomicin. Quiescent, 64% (21/33) control versus 45% (15/33) splitomicin, $P = 0.22$, two-tailed Fisher's exact test. Differentiation after division, 0% (0/33) control versus 18% (6/33) splitomicin, $P = 0.02$, two-tailed Fisher's exact test, $n = 23$ animals per group in six experiments. **g**, Schematic diagram representing the fates of OPCs after a cell division event. DMSO, dimethylsulfoxide.

extrinsic factors. To our knowledge, no different regional sources have been identified in the zebrafish spinal cord. However, regardless of the developmental origin of OPC subtypes, our data argue for an acquired rather than an intrinsic diversity, mainly because the determining criterion for the acquisition of distinct functional properties is the position of the respective OPC soma. Importantly, once an OPC had acquired a specific phenotype and/or function, it did not switch its role, meaning that the observed diversity of OPC properties reflects subtypes of cells that have functionally segregated rather than transitional states of the same cell type. The absence of intrinsic determinants of OPC diversity are in line with previous sequencing studies that reported that OPCs are initially a rather homogenous population, despite their different developmental origins, and that their diversification occurs with time^{10,12,18}. Our study extends these findings by showing that one subgroup of OPCs does not fully progress along its lineage, but instead indirectly contributes to the formation of myelinating oligodendrocytes by cell divisions to form a new OPC with a higher likelihood of differentiation.

What controls the differentiation of OPCs? In the mammalian CNS, the most notable differences in OPC differentiation capacity have been assigned to gray and white matter, which represent environments with different permissiveness for differentiation, believed to reflect the differing availability of myelination-competent axons⁹. In our system, the processes of all OPCs contact the same cohort

of axons, and only the OPC cell bodies reside in areas of different cellular densities. Axonal parameters such as caliber, presence or absence of inhibitory signals, and activity-dependent secreted factors are well-established regulators of axon ensheathment fate⁴¹. However, our data argue that these axonal signals are not sufficient to trigger OPC differentiation, a process that probably precedes axon choice for myelination. Our data highlight the importance of the local surroundings of the OPC cell body for the determination of its behavioral subtype and likelihood of its differentiation. This finding is of relevance to other models in which nuclear densities and axo-dendritic composition differ locally, including different layers of the mammalian cortex, where some OPCs differentiate while others do not, for reasons that are yet unclear. Future studies will be required to determine how the local environment of the OPC cell body affects its overall behavior, which may involve signaling molecules or local mechanical forces⁴².

Our data have revealed the importance of a recent cell division for OPC differentiation. The link between division and differentiation has been documented previously during mouse cortical development, in which the differentiation of an OPC occurs shortly after its last division^{43,44}. Other studies, however, report direct differentiation of OPCs in the adult mouse cortex, particularly in response to sensory enrichment and learning-associated oligodendrogenesis^{2,4,28}. It remains to be determined whether these differences

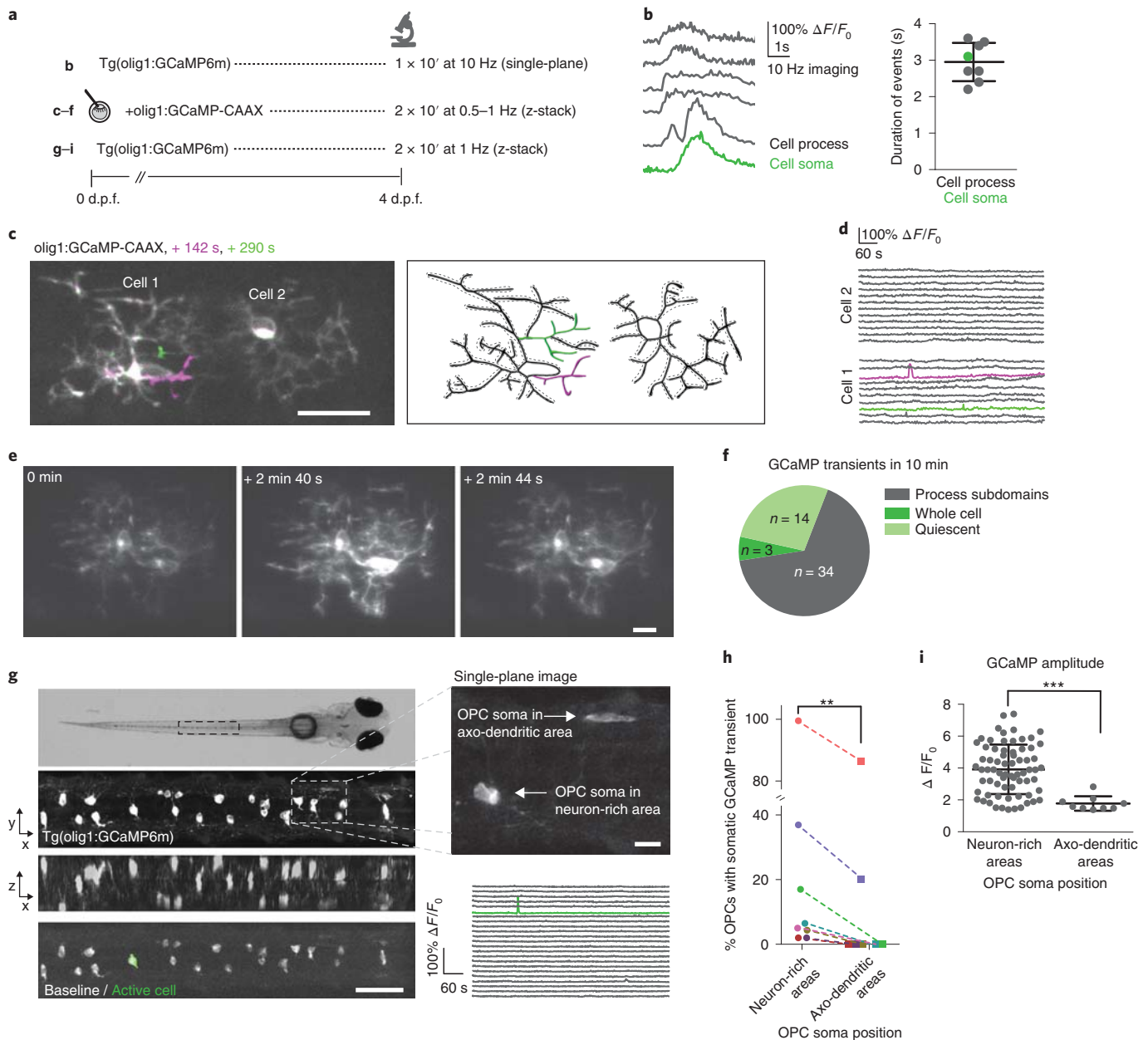


Fig. 6 | In vivo calcium imaging of individual OPCs. **a**, Overview of imaging conditions. **b**, Example traces of GCaMP transients in cell processes and soma of Tg(olig1:GCaMP6m) animals at 4 d.p.f. The average duration was 2.95 ± 0.5 s. $n = 6$ ROIs from two animals. **c**, Projection of three timepoints of two olig1:GCaMP-CAAX-expressing cells at 4 d.p.f., showing transients restricted to process subdomains. Example from 27 animals in 23 experiments. Scale bar, 20 μ m. Measured ROIs are indicated by dotted lines around the reconstructed cells. Active ROIs are highlighted in green and magenta. **d**, $\Delta F/F_0$ GCaMP transients of the different ROIs shown in **c**. **e**, Different time points of two individual olig1:GCaMP-CAAX-expressing cells showing transients spreading throughout the cells (example from cells as in **c**). Scale bar, 10 μ m. **f**, Quantification of different types of GCaMP transients observed during an observation period of 10 min in individual olig1:GCaMP-CAAX-expressing cells (n values as in **c**). **g**, Top: dorsal widefield view of a zebrafish at 4 d.p.f. Example of eight animals in eight experiments. Middle, z-projection and z-rotation of Tg(olig1:GCaMP6m) in the spinal cord as indicated by the boxed area above. Bottom: projection of two timepoints showing a GCaMP transient restricted to a single cell in the volume. Scale bar, 50 μ m. Top right: the inset depicts a single-plane image taken as indicated by the boxed area showing individual OPCs with their soma in neuron-rich and axo-dendritic areas. Scale bar, 10 μ m. Bottom right: $\Delta F/F_0$ GCaMP transients of all cells (green trace depicts active soma). **h**, Probability of somatic GCaMP transients in OPCs in neuron-rich and axo-dendritic areas at 4 d.p.f. (26% (73/285 cells) versus 19% (9/48 cells)); colors denote individual animals. $P = 0.007$, two-tailed Wilcoxon matched-pairs signed-rank test, $W = -36$, $n = 8$ animals in eight experiments. **i**, Quantification of GCaMP amplitudes measured in somata of OPCs in neuron-rich and axo-dendritic areas at 4 d.p.f. Data are expressed as mean \pm s.d. ($3.9 \pm 1.5 \Delta F/F_0$ versus $1.8 \pm 0.4 \Delta F/F_0$). $P < 0.001$, two-tailed Welch's t -test, $t = 8.894$, d.f. = 39.67, $n = 81$ and $n = 9$ cells, respectively, from eight animals in eight experiments.

represent peculiarities of developmental and adult myelination; whether differentiating OPCs in the adult are recently divided cells and therefore relatively young, or whether the enhanced oligodendrogenesis in adults results from enhanced integration of

differentiating cells rather than the triggering of differentiation. Although our data indicate that the likelihood of differentiation decreases as OPCs remain quiescent within the tissue, our study does not rule out the possibility that long-persisting OPCs can still

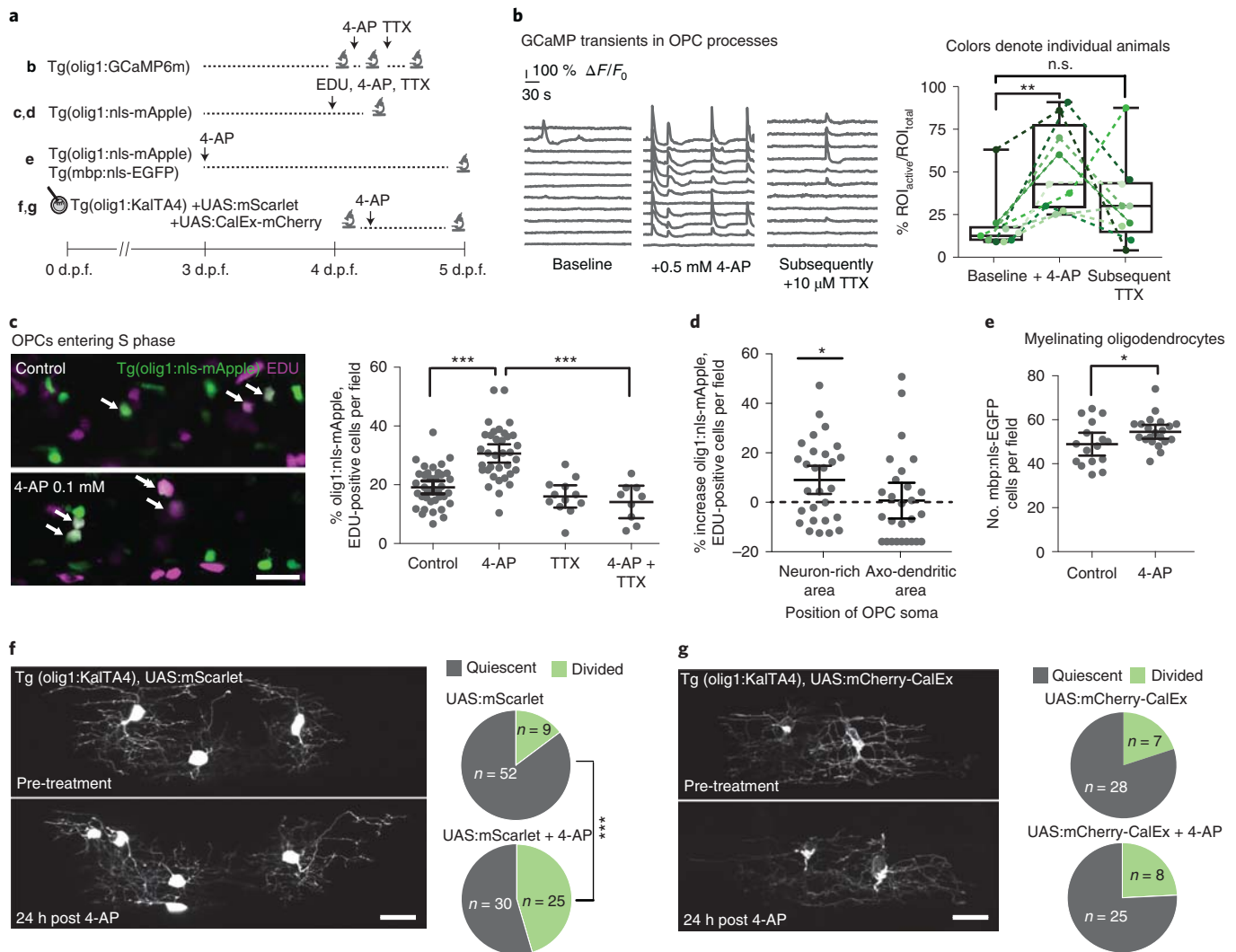


Fig. 7 | Manipulation of neural activity and OPC calcium signaling changes the proliferation of OPCs in neuron-rich areas. **a**, Overview of experimental paradigms. Lowercase bold letters refer to the figure panels in which data from each experiment are presented. **b**, Example GCaMP traces in *Tg(olig1:GCaMP6m)* at 4 d.p.f. before drug application, after treatment with 4-AP and after addition of TTX to the same animal. Quantification of GCaMP events (active ROIs/total ROIs) per fish in the different treatment conditions. Data are expressed as median \pm interquartile range, and whiskers represent minimum and maximum values (12.5% \pm 9.5/18.3 active ROIs before 4-AP, 42.8% \pm 28.6/78.0 after 4-AP, 30% \pm 14.1/44.1 after 4-AP and subsequent TTX). $P=0.004$ for control versus 4-AP, $P=0.23$ for 4-AP versus 4-AP + TTX, Friedman with Dunn's multiple comparison test, test statistic = 11.09, $n=9$ animals in five independent experiments. n.s., not significant. **c**, Representative confocal images of *Tg(olig1:nls-mApple)*, EDU-labeled OPCs at 4 d.p.f. Arrows indicate double-positive cells. Quantification shows *olig1:nls-mApple*-EDU double-positive cells in different treatment conditions. Data are expressed as mean \pm 95% confidence interval (19.1 \pm 1.1% in control, 30.6 \pm 1.5% in 4-AP, 14.1 \pm 2.2% in 4-AP + TTX). $P < 0.001$ for control versus 4-AP, $P < 0.001$ for 4-AP versus 4-AP + TTX, one-way ANOVA with Tukey's multiple comparison test, $F(3,89) = 22.44$, $n=37$, $n=35$ and $n=9$ animals from three experiments. Scale bar, 50 μm . **d**, Percentage increase in EDU-positive OPCs located in neuron-rich and axo-dendritic areas after 4-AP treatment. Each group in the graph is a comparison within itself (by plotting the difference in drug-treated group minus control for cells in both neuron-rich and axo-dendritic regions, respectively). Statistical testing was performed for drug-treated versus control groups (control groups are set to zero, indicated by dashed lines) in the respective areas. Data are expressed as mean \pm 95% confidence interval (9 \pm 3.1% versus 0.08 \pm 3.5%). $P=0.02$ in neuron-rich areas, two-tailed unpaired t -test, $t=2.431$, d.f. = 53, $n=28$ animals in three experiments. **e**, Myelinating oligodendrocyte numbers with and without 4-AP treatment. Data are expressed as mean \pm 95% confidence interval (48.9 \pm 2.4 cells per field in control versus 54.6 \pm 1.5 in 4-AP). $P=0.047$, two-tailed unpaired t -test, $t=2.058$, d.f. = 35, $n=16$ and $n=21$ animals in four experiments. **f**, Confocal images of individual OPCs at 4 d.p.f. and 24 h after 4-AP treatment. Scale bar, 20 μm . Pie charts show the frequency of cell divisions observed in the different conditions (15% (9/61 cells) in control versus 45% (25/55 cells) in 4-AP). $P < 0.001$, two-tailed Fisher's exact test, $n=18$ and $n=24$ animals. **g**, Confocal images of individual CalEx-expressing OPCs at 4 d.p.f. and 24 h after 4-AP treatment. Scale bar, 20 μm . Pie charts show the frequency of cell divisions observed in the different conditions (20% (7/35 cells) control versus 24% (8/33 cells) 4-AP). $P=0.77$, two-tailed Fisher's exact test, $n=11$ and $n=24$ animals.

differentiate. We found that OPCs that were committed to differentiate co-expressed markers of proliferation and differentiation, as shown by the appearance of *myrf* mRNA, a circumstance that is not established in mammals, although it has been noted¹⁸. We can only

speculate as to the reasons. As we detected comparatively low levels of *myrf* mRNA, it is possible that a functional protein may not yet have been present. Furthermore, because of the fast development of zebrafish and the high temporal resolution of our analysis, we may

have detected transitional stages of OPC differentiation that extend over longer periods of time in slower developing animals and that have therefore not been noted yet.

In our work, enhanced neural activity primarily increased OPC divisions. We cannot rule out the possibility that 4-AP also acts directly on OPCs, although the partial reversal of 4-AP-induced GCaMP transients by TTX in OPCs argues that this effect is at least partially induced by neurons. Activity-dependent stimulation of OPC proliferation has previously been observed after optogenetic stimulation of axonal firing and reversed by TTX injections to silence axons^{3,26}. We found that OPCs that were most sensitive to neural activity were not the cells that probably differentiate into myelinating oligodendrocytes, but were those that divide in response to activity. It is intriguing that the OPCs that most effectively integrate neural activity show elaborate process networks with major stable branches, in contrast to OPCs that readily differentiate and that remodel their entire process network within a short time. Synaptic contacts have been described between axons and OPCs⁴⁵, and it would make sense for such synaptic contacts to be localized along OPC processes that remain stable for some time. Consistent with this reasoning, it has been reported that synaptic connections between axons and OPCs are rapidly lost as OPCs differentiate^{21,46} and that axonal vesicle release regulates myelination through non-synaptic axon–OPCs contacts⁴⁷. These published findings and our own results suggest that synaptic axon–OPC contacts are not directly involved in regulating myelination (for example, by serving as a signaling hub to define the site of future ensheathment) because the OPCs that probably form synapses with axons are rarely the same cells that ultimately ensheath axons. What is the role of activity integration by OPCs? Our study shows that one role is the control of OPC numbers. However, because our data also show that a significant proportion of OPCs are not directly involved in generating new myelin, they raise the question of how else OPCs might use information from neurons to affect the brain. This question remains to be addressed in future studies.

Online content

Any methods, additional references, Nature Research reporting summaries, source data, extended data, supplementary information, acknowledgements, peer review information; details of author contributions and competing interests; and statements of data and code availability are available at <https://doi.org/10.1038/s41593-019-0581-2>.

Received: 11 June 2019; Accepted: 20 December 2019;

Published online: 17 February 2020

References

- Bergles, D. E. & Richardson, W. D. Oligodendrocyte development and plasticity. *Cold Spring Harb. Perspect. Biol.* **8**, a020453 (2015).
- Hughes, E. G., Orthmann-Murphy, J. L., Langseth, A. J. & Bergles, D. E. Myelin remodeling through experience-dependent oligodendrogenesis in the adult somatosensory cortex. *Nat. Neurosci.* **21**, 696–706 (2018).
- Gibson, E. M. et al. Neuronal activity promotes oligodendrogenesis and adaptive myelination in the mammalian brain. *Science* **344**, 1252304 (2014).
- McKenzie, I. A. et al. Motor skill learning requires active central myelination. *Science* **346**, 318–322 (2014).
- Zawadzka, M. et al. CNS-resident glial progenitor/stem cells produce Schwann cells as well as oligodendrocytes during repair of CNS demyelination. *Cell Stem Cell* **6**, 578–590 (2010).
- Emery, B. & Lu, Q. R. Transcriptional and epigenetic regulation of oligodendrocyte development and myelination in the central nervous system. *Cold Spring Harb. Perspect. Biol.* **7**, a020461 (2015).
- Liu, J., Moyon, S., Hernandez, M. & Casaccia, P. Epigenetic control of oligodendrocyte development: adding new players to old keepers. *Curr. Opin. Neurobiol.* **39**, 133–138 (2016).
- Foerster, S., Hill, M. F. E. & Franklin, R. J. M. Diversity in the oligodendrocyte lineage: plasticity or heterogeneity? *Glia* **67**, 1197–1205 (2019).
- Viganò, F. & Dimou, L. The heterogenic nature of NG2-glia. *Brain Res.* **1638**, 129–137 (2016).
- Marques, S. et al. Oligodendrocyte heterogeneity in the mouse juvenile and adult central nervous system. *Science* **352**, 1326–1329 (2016).
- Emery, B. & Barres, B. A. Unlocking CNS cell type heterogeneity. *Cell* **135**, 596–598 (2008).
- Marques, S. et al. Transcriptional convergence of oligodendrocyte lineage progenitors during development. *Dev. Cell* **46**, 504–517 (2018).
- Richardson, W. D., Young, K. M., Tripathi, R. B. & McKenzie, I. NG2-glia as multipotent neural stem cells: fact or fantasy? *Neuron* **70**, 661–673 (2011).
- Hill, R. A., Patel, K. D., Medved, J., Reiss, A. M. & Nishiyama, A. NG2 cells in white matter but not gray matter proliferate in response to PDGF. *J. Neurosci.* **33**, 14558–14566 (2013).
- Viganò, F., Möbius, W., Götz, M. & Dimou, L. Transplantation reveals regional differences in oligodendrocyte differentiation in the adult brain. *Nat. Neurosci.* **16**, 1370–1372 (2013).
- Falcão, A. M. et al. Disease-specific oligodendrocyte lineage cells arise in multiple sclerosis. *Nat. Med.* **24**, 1837–1844 (2018).
- Jäkel, S. et al. Altered human oligodendrocyte heterogeneity in multiple sclerosis. *Nature* **566**, 543–547 (2019).
- Spitzer, S. O. et al. Oligodendrocyte progenitor cells become regionally diverse and heterogeneous with age. *Neuron* **101**, 459–471 (2019).
- Sakry, D. et al. Oligodendrocyte precursor cells modulate the neuronal network by activity-dependent ectodomain cleavage of glial NG2. *PLoS Biol.* **12**, e1001993 (2014).
- Bergles, D. E., Roberts, J. D., Somogyi, P. & Jahr, C. E. Glutamatergic synapses on oligodendrocyte precursor cells in the hippocampus. *Nature* **405**, 187–191 (2000).
- De Biase, L. M., Nishiyama, A. & Bergles, D. E. Excitability and synaptic communication within the oligodendrocyte lineage. *J. Neurosci.* **30**, 3600–3611 (2010).
- Kukley, M., Capetillo-Zarate, E. & Dietrich, D. Vesicular glutamate release from axons in white matter. *Nat. Neurosci.* **10**, 311–320 (2007).
- Orduz, D. et al. Interneurons and oligodendrocyte progenitors form a structured synaptic network in the developing neocortex. *eLife* **4**, e06953 (2015).
- Kárádóttir, R., Cavalier, P., Bergersen, L. H. & Attwell, D. NMDA receptors are expressed in oligodendrocytes and activated in ischaemia. *Nature* **438**, 1162–1166 (2005).
- Chittajallu, R., Aguirre, A. & Gallo, V. NG2-positive cells in the mouse white and grey matter display distinct physiological properties. *J. Physiol.* **561**, 109–122 (2004).
- Barres, B. A. & Raff, M. C. Proliferation of oligodendrocyte precursor cells depends on electrical activity in axons. *Nature* **361**, 258–260 (1993).
- Makinodan, M., Rosen, K. M., Ito, S. & Corfas, G. A critical period for social experience-dependent oligodendrocyte maturation and myelination. *Science* **337**, 1357–1360 (2012).
- Xiao, L. et al. Rapid production of new oligodendrocytes is required in the earliest stages of motor-skill learning. *Nat. Neurosci.* **19**, 1210–1217 (2016).
- Schebesta, M. & Serluca, F. C. *olig1* expression identifies developing oligodendrocytes in zebrafish and requires hedgehog and notch signaling. *Dev. Dyn.* **238**, 887–898 (2009).
- Auer, F., Vagionitis, S. & Czopka, T. Evidence for myelin sheath remodeling in the CNS revealed by in vivo imaging. *Curr. Biol.* **28**, 549–559 (2018).
- Picelli, S. et al. Smart-seq2 for sensitive full-length transcriptome profiling in single cells. *Nat. Methods* **10**, 1096–1098 (2013).
- Chen, Y. et al. The oligodendrocyte-specific G protein-coupled receptor GPR17 is a cell-intrinsic timer of myelination. *Nat. Neurosci.* **12**, 1398–1406 (2009).
- Viganò, F. et al. GPR17 expressing NG2-glia: oligodendrocyte progenitors serving as a reserve pool after injury. *Glia* **64**, 287–299 (2015).
- Emery, B. et al. Myelin gene regulatory factor is a critical transcriptional regulator required for CNS myelination. *Cell* **138**, 172–185 (2009).
- Early, J. J. et al. An automated high-resolution in vivo screen in zebrafish to identify chemical regulators of myelination. *eLife* **7**, e35136 (2018).
- Kirschchuk, S., Scherer, J., Möller, T., Verkhatsky, A. & Kettenmann, H. Subcellular heterogeneity of voltage-gated Ca²⁺ channels in cells of the oligodendrocyte lineage. *Glia* **13**, 1–12 (1995).
- Pende, M., Holtzclaw, L. A., Curtis, J. L., Russell, J. T. & Gallo, V. Glutamate regulates intracellular calcium and gene expression in oligodendrocyte progenitors through the activation of DL-alpha-amino-3-hydroxy-5-methyl-4-isoxazolepropionic acid receptors. *Proc. Natl Acad. Sci. USA* **91**, 3215–3219 (1994).
- Krasnow, A. M., Ford, M. C., Valdivia, L. E., Wilson, S. W. & Attwell, D. Regulation of developing myelin sheath elongation by oligodendrocyte calcium transients in vivo. *Nat. Neurosci.* **93**, 1–28 (2017).
- Yu, X. et al. Reducing astrocyte calcium signaling in vivo alters striatal microcircuits and causes repetitive behavior. *Neuron* **99**, 1170–1187 (2018).

40. Dimou, L. & Simons, M. Diversity of oligodendrocytes and their progenitors. *Curr. Opin. Neurobiol.* **47**, 73–79 (2017).
41. Simons, M. & Lyons, D. A. Axonal selection and myelin sheath generation in the central nervous system. *Curr. Opin. Cell Biol.* **25**, 512–519 (2013).
42. Tsai, E. & Casaccia, P. Mechano-modulation of nuclear events regulating oligodendrocyte progenitor gene expression. *Glia* **67**, 1229–1239 (2019).
43. Zhu, X. et al. Age-dependent fate and lineage restriction of single NG2 cells. *Development* **138**, 745–753 (2011).
44. Hill, R. A., Patel, K. D., Goncalves, C. M., Grutzendler, J. & Nishiyama, A. Modulation of oligodendrocyte generation during a critical temporal window after NG2 cell division. *Nat. Neurosci.* **17**, 1518–1527 (2014).
45. Bergles, D. E., Jabs, R. & Steinhäuser, C. Neuron-glia synapses in the brain. *Brain Res. Rev.* **63**, 130–137 (2010).
46. Kukley, M., Nishiyama, A. & Dietrich, D. The fate of synaptic input to NG2 glial cells: neurons specifically downregulate transmitter release onto differentiating oligodendroglial cells. *J. Neurosci.* **30**, 8320–8331 (2010).
47. Wake, H. et al. Nonsynaptic junctions on myelinating glia promote preferential myelination of electrically active axons. *Nat. Commun.* **6**, 7844 (2015).

Publisher's note Springer Nature remains neutral with regard to jurisdictional claims in published maps and institutional affiliations.

© The Author(s), under exclusive licence to Springer Nature America, Inc. 2020

Methods

Zebrafish lines and husbandry. We used the following existing zebrafish lines and strains: Tg(mbp:nls-EGFP) (ref. 48), Tg(mbp:EGFP-CAAX)^{uc2Tg} (ref. 49), Tg(mbp:MA-Cerulean)^{tm101Tg} (ref. 30) (referred to here as Tg(mbp:memCerulean)), Tg(elavl3:HSA.h2b-GCaMP6s)^{h5Tg} (ref. 50) (here referred to as Tg(elavl3:h2b-GCaMP6s)), nacre and AB. The following lines were newly generated for this study: Tg(mfap4:memCerulean), Tg(olig1:GCaMP6m), Tg(olig1:KalTA4), Tg(olig1:memEYFP), Tg(olig1:nls-Cerulean), Tg(olig1:nls-mApple), Tg(mbp:KillerRed) and Tg(elavl3:synaptophysin-tagRFP). The *olig1* gene regulatory sequence used drives reporter gene expression in OPCs. As OPCs differentiate into myelinating oligodendrocytes, reporter expression is downregulated. All animals were kept at 28.5°C with a 14h–10h light–dark cycle according to local animal welfare regulations. All experiments carried out with zebrafish at protected stages have been approved by the government of Upper Bavaria (animal protocols AZ55.2-1-54-2532-199-2015 and AZ55.2-1-54-2532-200-2015 to T.C.).

Transgenesis constructs. Sequences for all primers used are listed in Supplementary Table 2. To generate the middle entry clones pME_GCaMP6m, pME_GCaMP6m-CAAX and pME_mCherry-CalEx, the respective coding sequences were PCR amplified from the template plasmids pGP-CMV-GCaMP6m (ref. 51) (gift from D. Kim and the Genetically-Encoded Neuronal Indicator and Effector project, Addgene plasmid 40754) and pZAC2.1_GfaABC₂D mCherry-hPMCA2w/b (ref. 39) (gift from B. Khakh) and recombined with pDONR221 using BP clonase (Invitrogen). The middle entry clone pME_synaptophysin-nostop was generated by BP reaction of the synaptophysin coding sequence that was PCR amplified from an existing template⁵² and recombined with pDONR221.

The middle entry clone pME_mScarlet was generated by BP recombination of mScarlet⁵³, for which the coding sequence with appropriate sites for recombination with pDONR221 was commercially synthesized by BioCat. The middle entry clone pME_KalTA4 has been published previously⁵⁴. The middle entry clones pME_nls-Cerulean and pME_nls-mApple were a gift from K. Kwan (University of Utah)⁵⁵. The 5' entry clone p5E_mfap4 was generated by PCR amplification of a 1.5 kb DNA fragment of *mfap4* upstream regulatory sequence⁵⁶ from AB genomic DNA and subsequent BP recombination into pDONR4P1R (Invitrogen). The 5' entry clone p5E_elavl3 has been published previously⁵⁷.

The expression constructs pTol2_10xUAS:mScarlet, pTol2_10xUAS:mCherry-CalEx, pTol2_olig1(4.2):nls-Cerulean, pTol2_olig1(4.2):nls-mApple and pTol2_olig1(4.2):KalTA4 were generated using the entry clones described above and additional entry clones of the Tol2Kit⁵⁵ using multisite LR recombination reactions. The expression constructs pTol2_olig1(4.2):memEYFP⁵⁰, pTol2_mbp:KillerRed⁵⁰ and pTol2_cntn1b:mCherry⁵⁸ have been published previously.

DNA microinjection for sparse labeling and generation of transgenic lines.

Fertilized zebrafish eggs were microinjected with 1 nl of an injection solution containing 5–25 ng μl^{-1} DNA, 25–50 ng μl^{-1} Tol2 transposase mRNA and 10% phenol red. Injected F0 animals were either used for single-cell analysis or raised to adulthood to generate full transgenic lines. For this, adult F0 animals were outcrossed with wild-type zebrafish, and F1 offspring were screened for germline transmission of the fluorescent transgene.

Pharmacological treatments. Zebrafish embryos at 3 and 4 d.p.f. were incubated in 4-AP (Sigma-Aldrich) and/or tetrodotoxin (TTX, Abcam) in Danieau's solution. For long-term treatments (6–48 h), 4-AP was used at 0.1 mM and TTX was used at 50 μM . For short-term treatments (<1 h), 4-AP was used at 0.5 mM and TTX at 10 μM . Embryos were incubated in splitomicin (Sigma-Aldrich) from 2 d.p.f. at 4–5 μM until analysis.

Tissue preparation and cryosectioning for histology. Zebrafish larvae (5- to 7-day-old) were euthanized with 4 mg ml^{-1} tricaine mesylate (PHARMAQ, UK) and immersion fixed overnight at 4°C in 4% paraformaldehyde. Fixed animals were cryoprotected for a minimum of 3 d in an increasing concentration of sucrose (10%, 20% and 30%), embedded in TissueTek and stored at –80°C until sectioning. Transverse sections of 14–16 μm thickness were cut using a Leica CM1850 UV cryostat and subsequently stored at –80°C until further use.

In situ hybridization. RNA probes against zebrafish *nkx2.2a* (NM_001308640; ACD, 529751), *cspg4* (ENSDART00000112782; ACD, 529741–C3), *myrf* (ENSDART00000157117; ACD, 574961–C2), *ptprz1b* (XM_005164526.4; ACD, custom-generated) and *gpr17* (ACD, 504601) were purchased from ACD. We used the RNAScope Multiplex Fluorescent V2 kit (ACD) on cryosections according to the manufacturer's protocol for fixed–frozen samples. Signals were detected using TSA-conjugated Opal dyes as listed in Supplementary Table 3 (PerkinElmer). After RNA hybridization, immunohistochemistry was carried out to detect transgenically expressed fluorescent proteins as described below.

Immunohistochemistry. All antibodies used are listed in Supplementary Table 3. First, sections were blocked for 1.5 h at room temperature (19–22°C) in PBS buffer, 0.1% Tween20, 10% FCS, 0.1% BSA and 3% normal goat serum. Primary

antibodies were incubated overnight at 4°C in blocking solution. Afterwards, sections were washed three times in PBS with 0.1% Tween20 and then incubated with appropriate Alexa Fluor (AF)-conjugated secondary antibodies (Invitrogen). Stained sections were washed two times in PBS with 0.1% Tween20 and once in PBS, and subsequently mounted with ProLong Diamond Antifade Mountant with DAPI (Thermo Fisher Scientific). Sections were stored at 4°C.

EDU incorporation assay. At 4 d.p.f., Tg(olig1:nls-mApple) zebrafish embryos were incubated in 0.4 mM EDU in Danieau's solution. After 6 h incubation, embryos were incubated for 15 min in 2 mg ml^{-1} Pronase (Sigma-Aldrich) and subsequently fixed for 2 h in 4% paraformaldehyde. Whole embryos and transverse spinal cord sections were stained for EDU using the Click-iT Edu Cell Proliferation Kit for Imaging with Alexa Fluor 647 dye (Thermo Fisher Scientific) as detailed in the kit protocol, with the exception of a 1.5 h Click-iT reaction incubation time. Afterwards, immunofluorescence staining was performed for transgene detection.

Mounting of embryonic and larval zebrafish for live-cell microscopy. Animals were either anaesthetized with 0.2 mg ml^{-1} tricaine mesylate or (in the case of GCaMP imaging) immobilized with 0.5 mg ml^{-1} of the non-depolarizing neuromuscular junction blocker mivacurium chloride (Abcam). For confocal microscopy, animals were mounted laterally in 1% ultrapure low melting point agarose (Invitrogen) on a glass coverslip. The coverslip was flipped over on a glass slide with a ring of high-vacuum grease filled with a drop of Danieau's solution to prevent drying out of the agarose. For lightsheet microscopy, embryos were mounted upright in low melting point agarose in a U-shaped glass capillary (Leica). After imaging, the animals were either euthanized or released from the agarose using microsurgery blades and kept individually until further use.

Confocal microscopy. Twelve-bit confocal images were acquired on Leica TCS SP8 laser scanning microscopes. We used a 405 nm wavelength for excitation of 4,6-diamidino-2-phenylindole (DAPI); 448 and 458 nm for excitation of Cerulean; 488 nm for eGFP and AF488; 514 nm for eYFP; 552 and 561 nm for mApple, mScarlet, mCherry, tagRFP and AF555; and 633 nm for AF633, AF647, Opal650 and BODIPY630/650. For fast confocal live-cell imaging of cell motility and GCaMP transients, we used an 8 kHz resonant scanner. All other acquisitions were carried out with a Galvo scanner. For overview images and analysis of cell numbers (that is, nuclear transgenes and EDU), we used 10 \times /0.4 NA (acquisition with 568 nm pixel size (xy) and 2 μm z-spacing) and 20 \times /0.7 NA (acquisition with 142 nm pixel size (xy) and 1 μm z-spacing) objectives. For analysis of stained cryosections, we used 63 \times /1.2 NA H₂O and 63 \times /1.3 NA glycerol objectives and acquired images with at least 100 nm pixel size (xy) and 1 μm z-spacing. For all other analyses, images were acquired using a 25 \times /0.95 NA H₂O objective with 114–151 nm pixel size (xy) and 1 μm z-spacing. When images were acquired for subsequent deconvolution, the x, y and z parameters were increased closer to Nyquist resolution to be compatible for processing with Huygens software (Scientific Volume Imaging).

Lightsheet microscopy. Lightsheet images were acquired with a Leica TCS SP8 Digital LightSheet using a 2.5 \times /0.07 NA illumination objective and 10 \times /0.3 NA and 25 \times /0.95 NA detection objectives with 2.5 mm deflection mirrors. Time-lapses of GCaMP fluorescence were acquired using a 488 nm excitation wavelength. A region of interest (ROI) was drawn around either individual cells or a portion (five to seven somites) of whole zebrafish spinal cord tissue. Time-lapses of z-stacks were acquired with a frame rate of 0.5–1 Hz for 2 \times 10 min, with a break of 10 min in between.

Assessment of zebrafish swimming behavior. Single 4 d.p.f. zebrafish were placed in a 3 cm dish in 3 ml of Danieau's solution (\pm 0.1 mM 4-AP and/or 50 μM TTX) and imaged for 2 min at 16 frames per s using a Hamamatsu Orca-05G camera equipped with a Kowa LM35JC10M objective.

Fluorescence activated cell sorting of single zebrafish OPCs. Approximately 2,000 Tg(olig1:memEYFP) fish at 5 d.p.f. were euthanized and de-yolked by repetitively pipetting of embryos in de-yolking buffer (55 mM NaCl, 1.2 mM KCl, 1.25 mM NaHCO₃) with a P1000 pipette tip. After two wash steps in Danieau's buffer and centrifugation for 1 minute at 300g, tissues were digested for 30 min at 37°C in a shaking incubator using the Papain Dissociation System kit (Worthington Biochemical Corporation) according to the manufacturer's instructions. The resulting cell pellet was resuspended in FACSmax Cell Dissociation Solution (Amsbio) with 5–10% FCS and filtered through a 30 μm Filcon syringe (BD Biosciences) before sorting. Sorting of olig1:memEYFP cells followed a two-step protocol using a MoFlo XDP cell sorter (Beckman Coulter). First, approximately 100,000 cells that were positive for eYFP and negative for propidium iodide (Thermo Fisher Scientific) were sorted to exclude dead cells. The resulting cell suspension was then sorted again for cells that were EYFP-positive and Vybrant DyeCycle Ruby (Thermo Fisher Scientific)-positive. Single cells were sorted into individual wells of a 384-well plate containing RNA lysis buffer for complementary DNA library preparation with the Smart-Seq2 protocol (provided

by the Eukaryotic Single-Cell Genomics Facility of the Karolinska Institutet, Stockholm), as described in previously published work³¹. Plates were stored at -80°C until further processing.

Single-cell RNA sequencing. Single-cell sequencing was performed on an Illumina HiSeq 2500 instrument with the following specifications. The run was performed on a high-output flow cell with 50bp single reads that were clustered using the HiSeq SR Cluster Kit v4 cBot and the HiSeq SBS Kit v4 50 cycle kit (Illumina). Reads were trimmed with Cutadapt 1.8.0 (ref. ⁵⁹) and aligned to the GRCz11 reference genome using STAR 2.5.1.b (ref. ⁶⁰) with ENSEMBL94 transcript annotations. The following parameters were used: `-sjdbFileChrStartEnd SJ.out.tab, -sjdbScore 0, -outFilterMatchNmin 10, -outSAMunmapped Within, -quantMode TranscriptomeSAM`, where SJ.out.tab was the splice junction database calculated by STAR on the same single cells in a first alignment. Aligned single-cell reads were sorted and transformed into bam files using Samtools 1.3. Gene expression was calculated with Salmon 0.9.1 (ref. ⁶¹) using the sorted bam files as input; from the outputs, we used the transcripts per million (TPM) gene expression values to build the expression matrix for the 384 cells. Alignment resulted in an average of 800,000 reads per cell and an average of 4,959 detected genes per cell.

Cells were clustered with Seurat 3 (ref. ⁶²) and filtered based on the distribution of gene expression (minimum 500 genes detected per cell) and mitochondrial gene expression (maximum 0.05%). The remaining 310 cells were log-normalized individually with a scale of factor of 10,000. For downstream analyses, we used the top 2,000 variable genes. The shared-nearest neighbor (SNN) graph was constructed on the cell-to-cell distance matrix from the top 50 principal components (PCs). The SNN graph with resolution 1 was used as input for the smart local moving algorithm to obtain cell clusters and visualized with t-distributed stochastic neighbor embedding (t-SNE). We identified five cell clusters, and the list of significantly differentially expressed genes (Wilcoxon rank sum test, $\text{min.pct} = 0.25$, $\text{thresh.use} = 0.25$, $\text{test.use} = \text{"wilcox"}$) in each cluster enabled us to identify two vascular leptomeningeal cell clusters, one oligodendrocyte cluster and two OPC clusters. Analysis of individual genes involved in proliferation and differentiation, such as *top2a*, *myrf* and *gpr17*, indicated that the expression of these genes was further segregated in subsets of cells within one of the OPC clusters. Specific markers for visualization on the t-SNE enabled us to identify three subclusters of OPCs that were later subset based on marker gene expression. A further increase in clustering resolution using the findclusters function from Seurat v3 resolution 2 corroborated the three OPC subclusters in an unsupervised manner (Supplementary Fig. 1a–c).

To measure the possible effect of cell cycle genes in the dataset, we retrieved all cell cycle genes from GO annotations from Biomart and the canonical human S phase and G2M phase gene list available at <https://satijalab.org/seurat> (Supplementary Fig. 1d–g). The human gene symbols and ENSEMBL annotations were transformed to zebrafish ortholog gene symbols using Biomart. For each cell, a score was calculated based on S phase and G2M phase gene expression using the Seurat v3 AddModuleScore function. The cell cycle score predicted the phase of each cell. Subclusters OPC_3 and OPC_4 were assigned to the G2M phase, and subcluster OPC_2 was assigned to the S and G2M phases (Supplementary Fig. 1h). To test for potential effects of cell cycle genes in our clustering, the data preprocessing was repeated, regressing out the cell cycle scores during the data scaling, in which the cell cycle PCs were removed. The final principal component analysis did not show segregation based on cell cycle (Supplementary Fig. 1i).

For subsequent analysis, we used the expression matrix that included the cell cycle genes. The SNN graph was constructed on the cell-to-cell distance matrix from the top ten PCs with the top 2,000 variable genes. The SNN graph with resolution 1 was used as an input for the smart local moving algorithm to obtain cell clusters and visualized with t-SNE. The resulting clusters corresponded to the previously defined clusters. Regressing out the cell cycle scores during data scaling did not lead to major changes in the main cell type clusters (Supplementary Fig. 1d).

GO term analysis of the different clusters was performed with ClueGO⁶³ using the top 30 upregulated genes within each cluster compared with all other clusters. We identified significantly enriched terms ($P < 0.05$) using a right-sided hypergeometric test for enrichment with a Benjamini–Hochberg P value correction and used the following databases: GO/Biological Processes (27 February 2019), GO/Molecular_Function (27 February 2019) and Reactome/Pathways (27 February 2019) for all GO Tree intervals using GO term fusion. Genes from each cluster were required to represent at least 1% of all genes within a GO term (with a minimal absolute number of $n = 2$ for OPC cluster #1, $n = 3$ for OPC cluster #4, $n = 6$ for OPC cluster #2 and $n = 7$ for OPC cluster #3) to be assigned to this cluster. The kappa score was always set to 0.4.

Analysis and presentation of imaging data. All data were analyzed using Fiji⁶⁴, Imaris 8.4.2 (Bitplane), Huygens Essential (v16.10 1p2), MATLAB r2017b, Microsoft Excel 2016, GraphPad Prism 6 and 7, Adobe Photoshop CS6 and Adobe Illustrator CS6. The Imaris FilamentTracer was used for three-dimensional reconstructions of OPC morphology. First, by tracing the entire process network of an individual OPC, we obtained information on total process length and branch point number of the cell. Second, we constructed a three-dimensional hull around

the filament network to obtain a measure of cell volume using the Surface Tool in Imaris. Cell complexity was expressed as the product of branch point density (branch point number divided by summed process length) and volume.

To analyze process remodeling dynamics of individual cells, cumulative maximum intensity time-projections of inverted grayscale images of OPC time-lapses were generated to obtain a measure of the percentage of stable processes at each time point relative to the starting time point. Measurements were performed using the Fiji plugin NeuronJ⁶⁵.

To trace GCaMP transients, ROIs were drawn using the Fiji ROI manager around the somata and/or processes of single cells. Traces of individual ROIs are shown as $\Delta F/F_0$ by expressing the maximum fluorescence intensity at each time point normalized to the first 100 frames of each ROI using a custom written Matlab script. GCaMP transients were counted as events when they were above 40% $\Delta F/F_0$ for the frequency of somatic transients and 30% $\Delta F/F_0$ for all other analyses. The duration of GCaMP transients is given as the half-width of the maximum $\Delta F/F_0$ for each event. To analyze changes in GCaMP frequency after pharmacological treatments, we used the mean intensity of GCaMP fluorescence traces in ROIs that were drawn around the same cells and/or processes in each treatment condition (baseline, after 4-AP and after TTX). For each ROI, fluorescence was normalized to the first 100 frames, and GCaMP events were determined using a threshold of 30% above average fluorescence change using the spike detrend function (<https://de.mathworks.com/help/finance/tsmovavg.html>).

Statistics and reproducibility. For analyses that involved cohorts of animals or treatment groups, zebrafish embryos of all conditions were derived from the same clutch and selected at random before treatment. No additional randomization was used during data collection. For time-lapse and cell fate analyses of OPCs, zebrafish were screened for single-cell labeling before imaging, and all animals with appropriate expression were used in the experiment. Data collection and analysis were not performed blind, owing to the conditions of the experiments. No data were excluded from the analyses.

We selected sample sizes based on similar sample sizes that we and others have previously reported for similar experiments^{38,58,66–68}. No statistical analysis was used to pre-determine sample sizes. Analyses were performed with Microsoft Excel and GraphPad Prism. All data were tested for normal distribution using the Shapiro–Wilk normality test before statistical testing. In the figures, normally distributed data are shown as mean \pm standard deviation (s.d.) or with 95% confidence intervals, whereas non-normally distributed data are shown as median with 25% and 75% percentiles. For statistical tests of normally distributed data that compared two groups, we used unpaired t -tests. Non-normally distributed data were tested for statistical significance using the Mann–Whitney U test (unpaired data) or the Wilcoxon signed-rank test (paired data). To compare more than two groups, analysis of variance (ANOVA) was used in combination with Tukey's (parametric) or Dunn's (non-parametric) multiple comparisons test (Friedman for paired data, Kruskal–Wallis for unpaired data). We used Fisher's exact test to analyze contingency tables.

Reporting Summary. Further information on research design is available in the Nature Research Reporting Summary linked to this article.

Data availability

Raw sequence data, gene expression data and cell type annotation tables have been deposited in the Gene Expression Omnibus under accession number GSE132166. A web resource is available at <https://ki.se/en/mbb/oligointernode>. The data that support the findings of this study are available from the corresponding author upon reasonable request.

References

- Karttunen, M. J., Czopka, T., Goedhart, M., Early, J. J. & Lyons, D. A. Regeneration of myelin sheaths of normal length and thickness in the zebrafish CNS correlates with growth of axons in caliber. *PLoS ONE* **12**, e0178058 (2017).
- Almeida, R. G., Czopka, T., French-Constant, C. & Lyons, D. A. Individual axons regulate the myelinating potential of single oligodendrocytes in vivo. *Development* **138**, 4443–4450 (2011).
- Freeman, J. et al. Mapping brain activity at scale with cluster computing. *Nat. Methods* **11**, 941–950 (2014).
- Chen, T.-W. et al. Ultrasensitive fluorescent proteins for imaging neuronal activity. *Nature* **499**, 295–300 (2013).
- Meyer, M. P. & Smith, S. J. Evidence from in vivo imaging that synaptogenesis guides the growth and branching of axonal arbors by two distinct mechanisms. *J. Neurosci.* **26**, 3604–3614 (2006).
- Bindels, D. S. et al. mScarlet: a bright monomeric red fluorescent protein for cellular imaging. *Nat. Methods* **14**, 53–56 (2017).
- Almeida, R. G. & Lyons, D. A. Intersectional gene expression in zebrafish using the split KalTA4 system. *Zebrafish* **12**, 377–386 (2015).
- Kwan, K. M. et al. The Tol2kit: a multisite gateway-based construction kit for Tol2 transposon transgenesis constructs. *Dev. Dyn.* **236**, 3088–3099 (2007).

56. Walton, E. M., Cronan, M. R., Beerman, R. W. & Tobin, D. M. The macrophage-specific promoter *mfap4* allows live, long-term analysis of macrophage behavior during mycobacterial infection in zebrafish. *PLoS ONE* **10**, e0138949 (2015).
57. Mensch, S. et al. Synaptic vesicle release regulates myelin sheath number of individual oligodendrocytes in vivo. *Nat. Neurosci.* **18**, 628–630 (2015).
58. Czopka, T., French-Constant, C. & Lyons, D. A. Individual oligodendrocytes have only a few hours in which to generate new myelin sheaths in vivo. *Dev. Cell* **25**, 599–609 (2013).
59. Martin, M. Cutadapt removes adapter sequences from high-throughput sequencing reads. *EMBnet J.* **17**, 10–12 (2011).
60. Dobin, A. et al. STAR: ultrafast universal RNA-seq aligner. *Bioinformatics* **29**, 15–21 (2013).
61. Patro, R., Duggal, G., Love, M. I., Irizarry, R. A. & Kingsford, C. Salmon provides fast and bias-aware quantification of transcript expression. *Nat. Methods* **14**, 417–419 (2017).
62. Butler, A., Hoffman, P., Smibert, P., Papalexi, E. & Satija, R. Integrating single-cell transcriptomic data across different conditions, technologies, and species. *Nat. Biotechnol.* **36**, 411–420 (2018).
63. Bindea, G. et al. ClueGO: a Cytoscape plug-in to decipher functionally grouped gene ontology and pathway annotation networks. *Bioinformatics* **25**, 1091–1093 (2009).
64. Schindelin, J. et al. Fiji: an open-source platform for biological-image analysis. *Nat. Methods* **9**, 676–682 (2012).
65. Meijering, E. et al. Design and validation of a tool for neurite tracing and analysis in fluorescence microscopy images. *Cytometry A* **58**, 167–176 (2004).
66. Hines, J. H., Ravanelli, A. M., Schwandt, R., Scott, E. K. & Appel, B. Neuronal activity biases axon selection for myelination in vivo. *Nat. Neurosci.* **18**, 683–689 (2015).
67. Kirby, B. B. et al. In vivo time-lapse imaging shows dynamic oligodendrocyte progenitor behavior during zebrafish development. *Nat. Neurosci.* **9**, 1506–1511 (2006).
68. Baraban, M., Koudelka, S. & Lyons, D. A. Ca²⁺ activity signatures of myelin sheath formation and growth in vivo. *Nat. Neurosci.* **19**, 1–23 (2017).

Acknowledgements

We are grateful to R. Almeida, D. Lyons, T. Misgeld, M. Simons and all members of the Czopka laboratory for their comments and suggestions during the assembly of the

data and their presentation in this manuscript. We thank B. Khakh (Department of Physiology, University of California, Los Angeles) for providing the CalEx plasmid before publication, K. Kwan (Department of Human Genetics, University of Utah) for providing the pME_nls-Cerulean and pME_nls-mApple plasmids, and D. Kim (Howard Hughes Medical Institute, Janelia Research Campus) for providing the GCaMP6m plasmid. We thank the Single Cell Genomics Facility, the Science for Life Laboratory, the National Genomics Infrastructure and UPPMAX for providing assistance with massive parallel sequencing and computational infrastructure. The bioinformatics computations were performed on resources provided by the Swedish National Infrastructure for Computing at UPPMAX, Uppsala University. E.A. is funded by the European Union (Horizon 2020 Research and Innovation Programme, Marie Skłodowska-Curie actions, grant SOLO, number 794689). Work in G.C.-B.'s research group was supported by the Swedish Research Council (grant 2015-03558), the European Union (Horizon 2020 Research and Innovation Programme, European Research Council Consolidator Grant EPISCOPE, grant 681893), the Swedish Brain Foundation (FO2017-0075), the Ming Wai Lau Centre for Reparative Medicine and the Karolinska Institutet. Work in T.C.'s research group was funded by a Starting Grant from the European Research Council (ERC StG MecMy, grant 714440), the Deutsche Forschungsgemeinschaft through its Emmy Noether Programme for young investigators (ENP CZ226/1-1) and the Deutsche Forschungsgemeinschaft Excellence Strategy within the framework of the Munich Cluster for Systems Neurology (EXC 2145 SyNergy-D 390857198).

Author contributions

T.H., R.M., L.J.H., W.B., G.C.-B. and T.C. designed the experiments. T.H., R.M., L.J.H., W.B. and F.A. conducted the experiments. T.H., R.M., L.J.H. and T.C. analyzed the imaging data. E.A. and G.C.-B. performed the bioinformatic analysis of RNA sequencing data. T.C. conceived the project and wrote the manuscript with input from all authors.

Competing interests

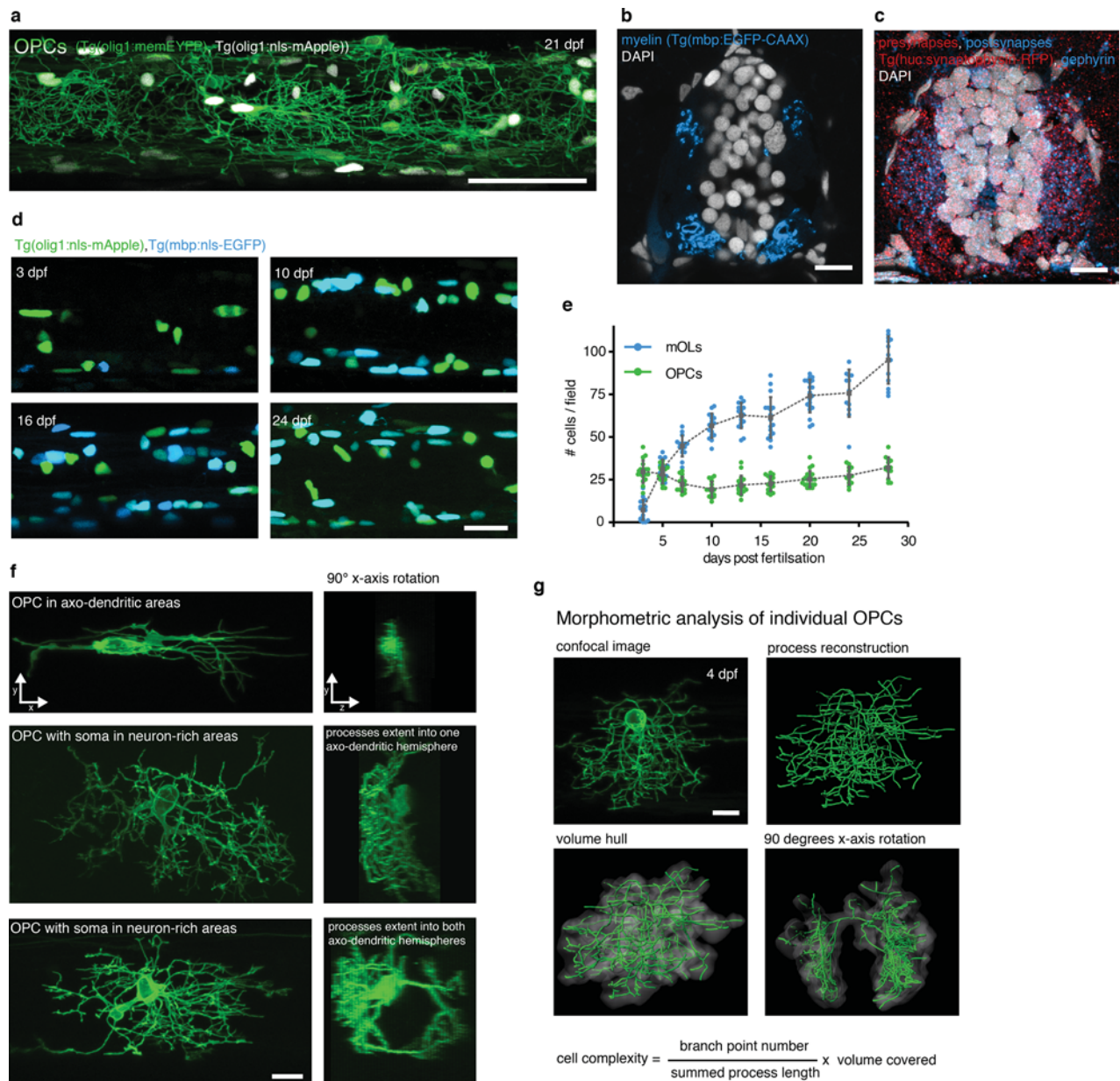
The authors declare no competing interests.

Additional information

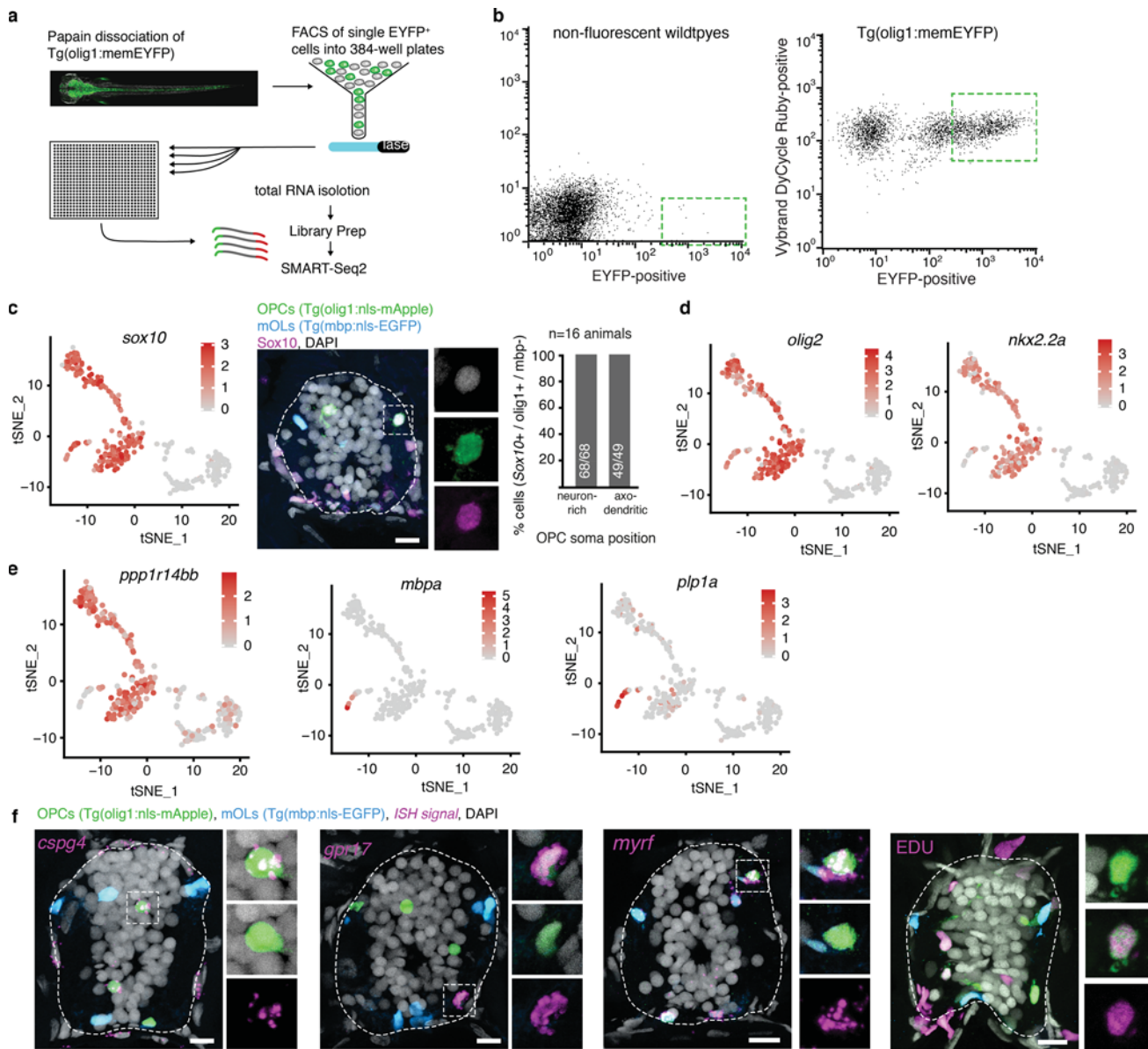
Supplementary information is available for this paper at <https://doi.org/10.1038/s41593-019-0581-2>.

Correspondence and requests for materials should be addressed to T.C.

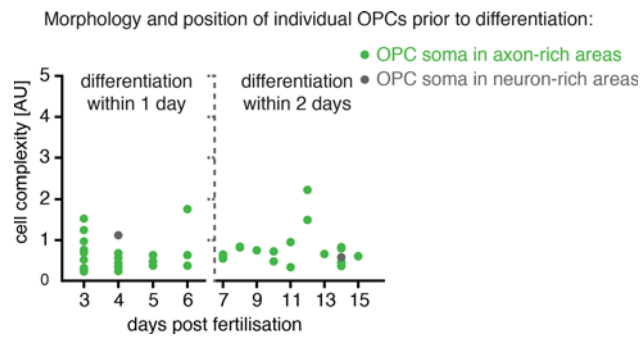
Reprints and permissions information is available at www.nature.com/reprints.



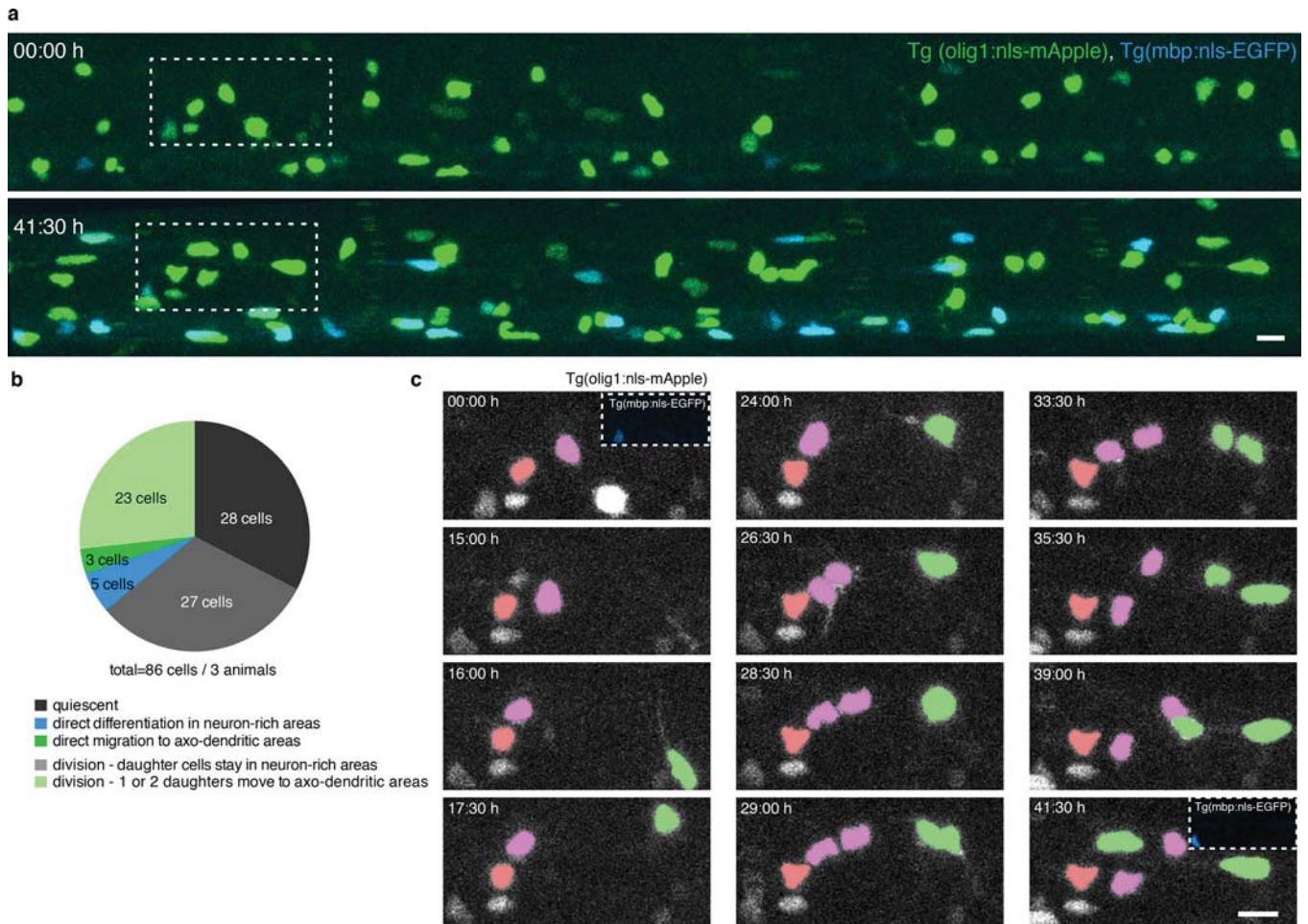
Extended Data Fig. 1 | Characterization of OPCs in the zebrafish spinal cord. **a**, Confocal image of a Tg(olig1:memEYFP),Tg(olig1:nls-mApple) zebrafish at the level of the spinal cord at 21 d.p.f. (example of three animals from one experiment). Scale bar, 50 μm . **b**, Cross-sectional view of the spinal cord showing the distribution of myelin in Tg(mbp:EGFP-CAAX) at 7 d.p.f. (example of 12 animals from four experiments). Scale bar, 10 μm . **c**, Cross-sectional view of the spinal cord showing the distribution of pre- and postsynapses (Tg(elavl3:synaptophysin-RFP), anti-mCherry, anti-gephyrin) at 7 d.p.f. (example of 12 animals from four experiments). Scale bar, 10 μm . **d**, Confocal images of Tg(mbp:nls-EGFP),Tg(olig1:nls-mApple) transgenic animals between 4 and 28 d.p.f. (n values as in **e**). Scale bar, 20 μm . **e**, Cell numbers of OPCs (olig1: nls-mApple-positive, mbp:nls-EGFP-negative) and myelinating oligodendrocytes (mbp:nls-EGFP-positive) in the spinal cord. Data are expressed as mean cells per field \pm s.d. at 3 ($n=17$ animals in two experiments), 5 ($n=15$ animals in three experiments), 7 ($n=15$ in three experiments), 10 ($n=16$ in three experiments), 13 ($n=17$ in two experiments), 16 ($n=17$ in two experiments), 20 ($n=20$ in three experiments), 24 ($n=12$ in three experiments) and 28 ($n=13$ in three experiments) d.p.f. **f**, Example images of individual OPCs showing a range of morphologies. The soma can be localized within axo-dendritic (top) or neuron-rich areas (middle, bottom). The process network of an individual cell can be restricted to one side of the spinal cord (top and middle cells), but it can also reach to both sides of the spinal cord (bottom cell) (n values as in **g**). Scale bar, 10 μm . **g**, OPC morphometry using three-dimensional process tracing and creation of a volume hull around the reconstructed filaments ($n=228$ cells from 56 animals between 3 and 16 d.p.f. in 24 experiments). Scale bar, 10 μm .



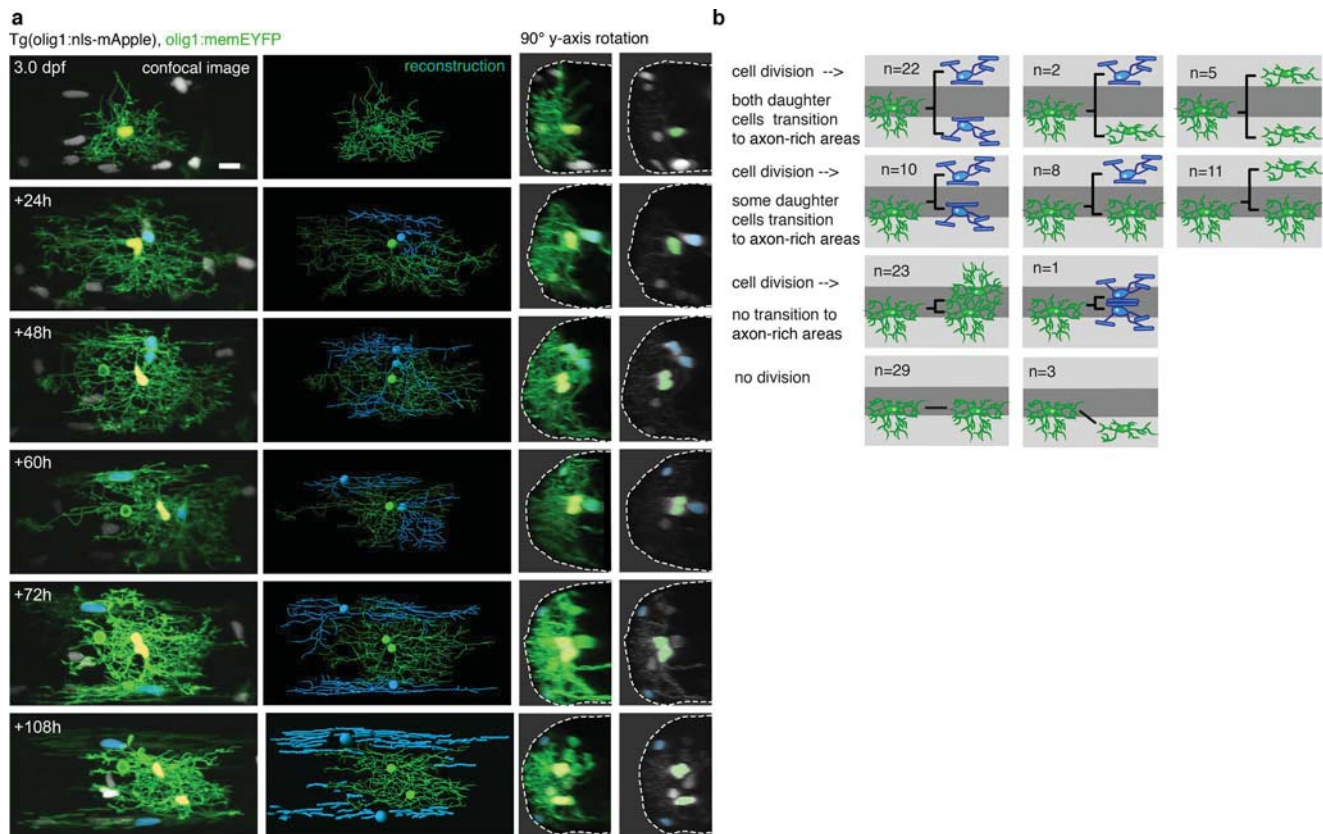
Extended Data Fig. 2 | Analysis of single-cell RNA sequencing clusters. a, Schematic overview of cell isolation, sorting and sequencing. **b**, Flow cytometry plots of olig1:memEYFP-sorted cells and wild-type control cells. Dotted lines indicate the gating used (example from two independent experiments). **c**, t-SNE plot showing expression of *sox10* (total sample size $n=310$ cells). Immunohistochemistry for *sox10* on transverse spinal cord sections of 7 d.p.f. Tg(olig1:nls-mApple), Tg(mbp:nls-EGFP) animals and quantification of *sox10*-expressing OPCs (olig1:nls-mApple-positive, mbp:nls-EGFP-negative) in neuron-rich and axo-dendritic areas (100% (68/68) versus 100% (49/49) positive cells, $n=16$ animals in four experiments). Dotted lines indicate the outlines of the spinal cord. Scale bar, 10 μ m. **d**, t-SNE plot showing expression of *olig2* and *nkx2.2a* (sample size as in **c**). **e**, t-SNE plot showing expression of *ppp1r14bb*, *mbpa* and *plp1a* (sample size as in **c**). **f**, Confocal images with in situ hybridizations for *cspg4*, *gpr17*, *myrf*, and labeling of EDU incorporated cells on transverse spinal cord sections of 7 d.p.f. Tg(olig1:nls-mApple), Tg(mbp:nls-EGFP) animals (see Fig. 2e,i,k,l for respective n values). Scale bar, 10 μ m.



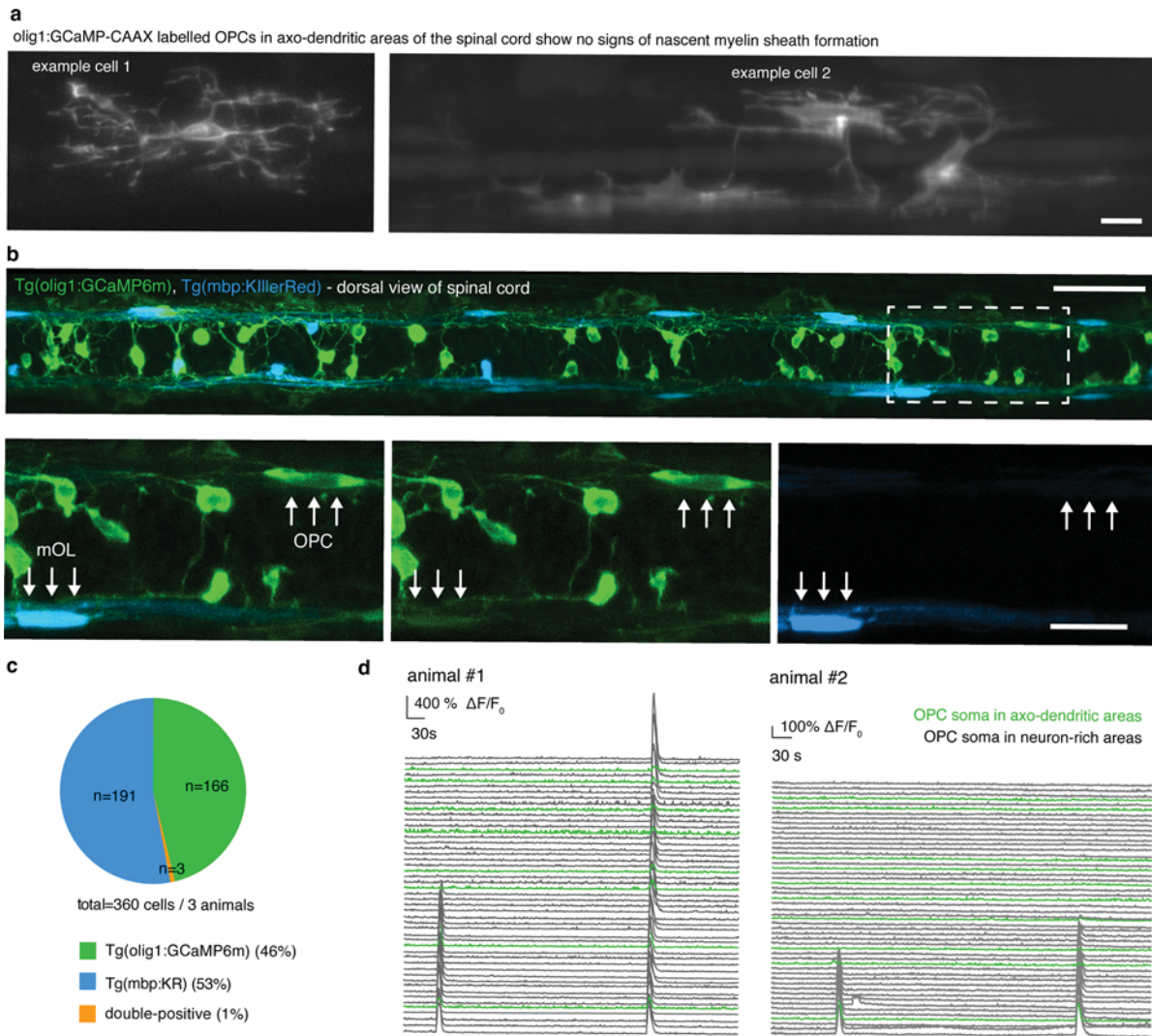
Extended Data Fig. 3 | Quantification of OPC morphology and position before differentiation. Quantification of OPC complexity and soma position from imaging timelines between 3 and 15 d.p.f. Measured is the last timepoint as OPC before differentiation, as assessed by myelin sheath formation (imaging intervals of 1 d between 3 and 7 d.p.f., and 2 d between 7 and 15 d.p.f.). $n = 10$, $n = 6$, $n = 3$, $n = 3$, $n = 3$, $n = 2$, $n = 1$, $n = 2$, $n = 2$, $n = 2$, $n = 1$, $n = 5$ and $n = 1$ cells at 3, 4, 5, 6, 7, 8, 9, 10, 11, 12, 13, 14 and 15 d.p.f. Data from 23 animals in six experiments.



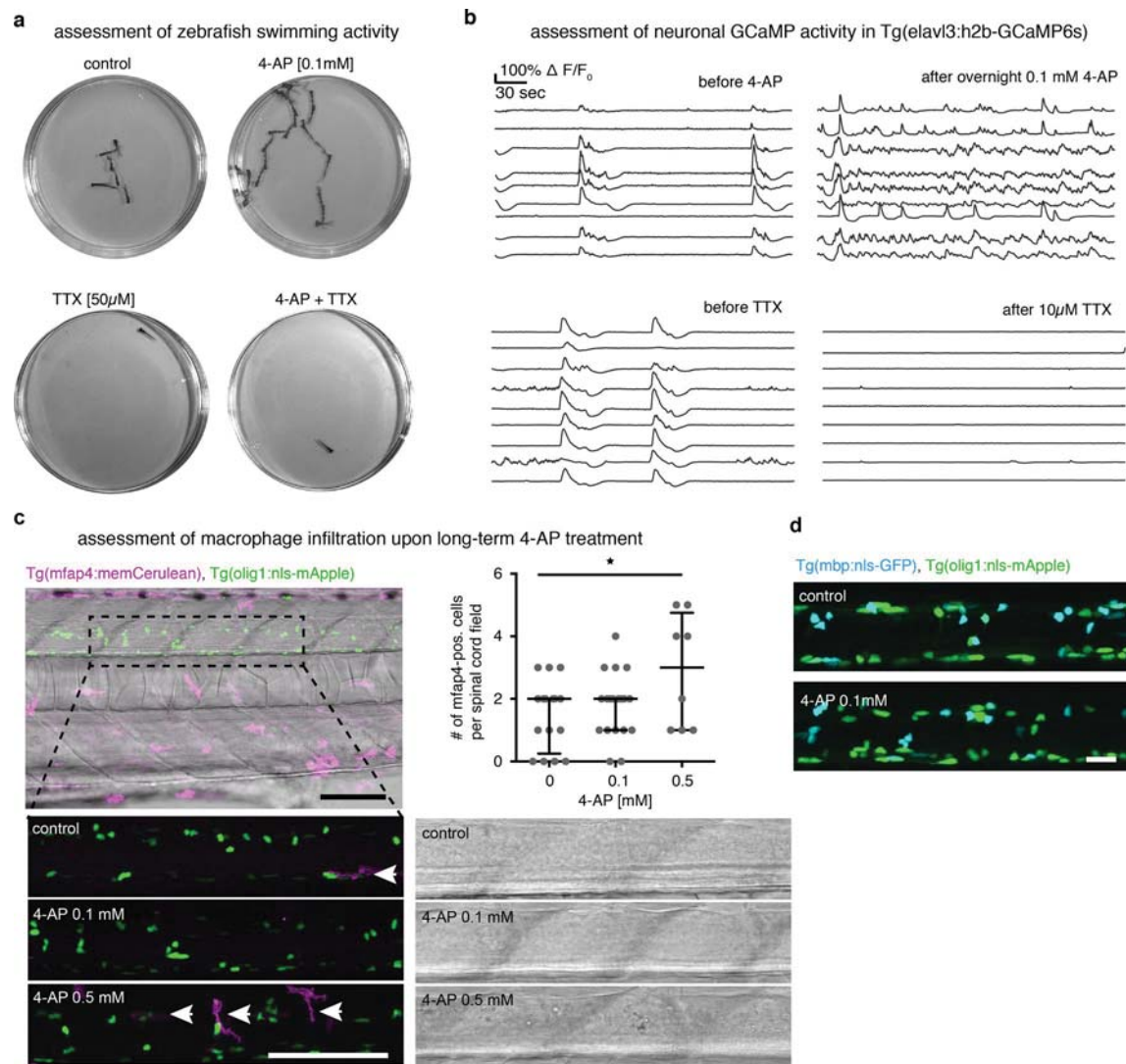
Extended Data Fig. 4 | Time-lapse imaging of OPC population dynamics. **a**, Overview images of transgenic zebrafish labeling nuclei of OPCs (olig1:nls-mApple) and myelinating oligodendrocytes (mbp:nls-EGFP) at the beginning and end of a timelapse between 3 and 5 d.p.f. Dashed boxes indicate the areas shown in panel c ($n=3$ animals in two experiments). Scale bar, 10 μm . **b**, Quantification of the fates of OPCs found in neuron-rich areas. A detailed breakdown of the data shown in Fig. 4e. **c**, Zoom-ins and false coloring of the time-lapse in **a**, showing potential behaviors of OPCs in neuron-rich areas: remaining quiescent (red cell), generating new OPCs in neuron-rich areas (magenta cells) or generating new OPCs in axo-dendritic areas (green cells). The insets at the first and last timepoints show the absence of myelin markers (mbp:nls-EGFP) in the cells studied ($n=3$ animals in two experiments). Scale bar, 10 μm .



Extended Data Fig. 5 | Cell fate analysis of OPCs with their soma in neuron-rich areas. **a**, Time series of an individual OPC with its soma in neuron-rich areas that gives rise to myelinating oligodendrocytes by proliferation-mediated generation of daughter OPCs in axo-dendritic areas. Left panel, confocal images. Middle panel, reconstructions of the starting cell and the individual daughter cells. Cells that will differentiate are shown in blue. Right panels, y-axis rotations showing olig1:nls-mApple cell body positions within the hemi-spinal cord. Dashed lines depict the outline of the spinal cord. One of eight examples from seven animals in six experiments. Scale bar, 10 μ m. **b**, Graphical summary of cell fates from the data analyzed in Fig. 5a-d. See also Supplementary Fig. 2.



Extended Data Fig. 6 | Characterization of OPC GCaMP reporter lines. **a**, Example images of individual olig1:GCaMP-CAAX-labeled OPCs in axo-dendritic areas of the zebrafish spinal cord at 4 d.p.f. The absence of nascent ensheathments indicates that these cells are not early differentiating oligodendrocytes ($n = 9$ independent experiments). Scale bar, 10 μm . **b**, Dorsal views of Tg(olig1:GCaMP6m),Tg(mbp:KillerRed) transgenic zebrafish at 4 d.p.f. to label OPCs and differentiated oligodendrocytes. Dotted box indicates position of zoom-ins in bottom row ($n = 3$ animals in one experiment). Scale bars, 50 μm (top) and 20 μm (bottom). **c**, Quantification of single- and double-positive cells from images as shown in **b**. **d**, $\Delta F/F_0$ GCaMP transients of individual cells in two Tg(olig1:GCaMP6m) zebrafish. Green traces depict cells in axo-dendritic areas, and gray traces depict cells in neuron-rich areas (total of eight animals in eight experiments).



Extended Data Fig. 7 | Effects of chronic 4-AP incubation on zebrafish. **a**, Minimum intensity projections of a 2 min time-lapse of fish freely swimming in a 3 cm petri dish in different treatment conditions ($n=6$, $n=7$, $n=3$ and $n=3$ animals in control, 4-AP, TTX and 4-AP+TTX conditions, three independent experiments). **b**, Traces of GCaMP transients from Tg(elavl3:h2b-GCaMP6s) zebrafish at 4 d.p.f. and after overnight incubation in 0.1 mM 4-AP and before and after 10 μ M TTX (seven animals per condition in two experiments). **c**, Confocal images of Tg(mfap4:memCerulean), Tg(olig1:nls-mApple) zebrafish at 4 d.p.f. after treatment with 0.1 mM 4-AP, 0.5 mM 4-AP, or Danieau's solution as a control. Transmitted light images show spinal cord morphology and tissue integrity after drug treatment. Scale bars, 100 μ m. The graph shows the number of macrophages that accumulate in a 400 μ m length of spinal cord of Tg(mfap4:memCerulean) zebrafish after 1 d of control ($2 \pm 0.25/2$ cells), 0.1 mM ($2 \pm 1/2$ cells) and 0.5 mM ($3 \pm 0.25/2$ cells) 4-AP treatment (median \pm 25%/75% percentiles). $P=0.43$ (control versus 0.1 mM 4-AP), $P=0.03$ (control versus 0.5 mM 4-AP), Kruskal-Wallis test, test statistic=3.003, $n=16$, $n=19$ and $n=8$ animals in three experiments. **d**, Representative images of Tg(mbp:nls-EGFP), Tg(olig1:nls-mApple) zebrafish in control treatment and after 2 d of 0.1 mM 4-AP treatment (see Fig. 7e for n values). Scale bar, 20 μ m.

Reporting Summary

Nature Research wishes to improve the reproducibility of the work that we publish. This form provides structure for consistency and transparency in reporting. For further information on Nature Research policies, see [Authors & Referees](#) and the [Editorial Policy Checklist](#).

Statistics

For all statistical analyses, confirm that the following items are present in the figure legend, table legend, main text, or Methods section.

n/a Confirmed

- The exact sample size (n) for each experimental group/condition, given as a discrete number and unit of measurement
- A statement on whether measurements were taken from distinct samples or whether the same sample was measured repeatedly
- The statistical test(s) used AND whether they are one- or two-sided
Only common tests should be described solely by name; describe more complex techniques in the Methods section.
- A description of all covariates tested
- A description of any assumptions or corrections, such as tests of normality and adjustment for multiple comparisons
- A full description of the statistical parameters including central tendency (e.g. means) or other basic estimates (e.g. regression coefficient) AND variation (e.g. standard deviation) or associated estimates of uncertainty (e.g. confidence intervals)
- For null hypothesis testing, the test statistic (e.g. F , t , r) with confidence intervals, effect sizes, degrees of freedom and P value noted
Give P values as exact values whenever suitable.
- For Bayesian analysis, information on the choice of priors and Markov chain Monte Carlo settings
- For hierarchical and complex designs, identification of the appropriate level for tests and full reporting of outcomes
- Estimates of effect sizes (e.g. Cohen's d , Pearson's r), indicating how they were calculated

Our web collection on [statistics for biologists](#) contains articles on many of the points above.

Software and code

Policy information about [availability of computer code](#)

Data collection

LASX 3.5.2.18963 (Leica), Illumina HiSeq2500, Summit v5.2 (for MoFlo XDP Beckmann Coulter)

Data analysis

Fiji v1.52o, Imaris 8.4.2 (Bitplane), NeuronJ (plugin for Fiji, open source), Huygens Essential 18.10 (Scientific Volume Imaging), Matlab R2018b (MathWorks), Microsoft Excel 2016 (Microsoft), Prism 7.03 (GraphPad), Photoshop CS6 v13.0.1 x64 (Adobe), Illustrator CS6 16.0.0 (Adobe), Summit v5.2 software (for MoFlo XDP Beckmann Coulter), FlowJo v10 (Becton Dickinson), Cytoscape 3.7.1 (open source), ClueGo (plugin for Cytoscape, Open Source), STAR 2.5.1.b (open source), Salmon 0.9.1 (open source), Samtools 1.3 (open source), Seurat 3 (open source),

For manuscripts utilizing custom algorithms or software that are central to the research but not yet described in published literature, software must be made available to editors/reviewers. We strongly encourage code deposition in a community repository (e.g. GitHub). See the Nature Research [guidelines for submitting code & software](#) for further information.

Data

Policy information about [availability of data](#)

All manuscripts must include a [data availability statement](#). This statement should provide the following information, where applicable:

- Accession codes, unique identifiers, or web links for publicly available datasets
- A list of figures that have associated raw data
- A description of any restrictions on data availability

The data that support the findings of this study are available from the corresponding author upon reasonable request. Raw sequence data, gene expression and cell type annotation tables have been deposited in the Gene Expression Omnibus (GEO) under accession number GSE132166. A webresource is available at <https://ki.se/en/mbb/oligointernode>. Any specific code for the scRNA-seq data analysis can be found at <https://github.com/Castelo-Branco-lab/>

Field-specific reporting

Please select the one below that is the best fit for your research. If you are not sure, read the appropriate sections before making your selection.

Life sciences Behavioural & social sciences Ecological, evolutionary & environmental sciences

For a reference copy of the document with all sections, see [nature.com/documents/nr-reporting-summary-flat.pdf](https://www.nature.com/documents/nr-reporting-summary-flat.pdf)

Life sciences study design

All studies must disclose on these points even when the disclosure is negative.

Sample size	No sample-size calculations were performed. Sample size was determined to be adequate based on the consistency of measurable differences between groups and were deemed sufficient to support the conclusion.
Data exclusions	No data were excluded from analysis.
Replication	All experiments were repeated at least 3 times and results could be replicated each time.
Randomization	For drug treatment, zebrafish embryos were chosen at random from a clutch and added to wells of a plate containing drug or control solution.
Blinding	Investigators were not blinded during data collection and analysis. Descriptive imaging data that do not compare groups cannot be blinded. When treatment groups have been compared, internal cross-counting by group members who did not perform the experiment has been performed for all experiments at random.

Reporting for specific materials, systems and methods

We require information from authors about some types of materials, experimental systems and methods used in many studies. Here, indicate whether each material, system or method listed is relevant to your study. If you are not sure if a list item applies to your research, read the appropriate section before selecting a response.

Materials & experimental systems

n/a	Involvement in the study
<input type="checkbox"/>	<input checked="" type="checkbox"/> Antibodies
<input checked="" type="checkbox"/>	<input type="checkbox"/> Eukaryotic cell lines
<input checked="" type="checkbox"/>	<input type="checkbox"/> Palaeontology
<input type="checkbox"/>	<input checked="" type="checkbox"/> Animals and other organisms
<input checked="" type="checkbox"/>	<input type="checkbox"/> Human research participants
<input checked="" type="checkbox"/>	<input type="checkbox"/> Clinical data

Methods

n/a	Involvement in the study
<input checked="" type="checkbox"/>	<input type="checkbox"/> ChIP-seq
<input type="checkbox"/>	<input checked="" type="checkbox"/> Flow cytometry
<input checked="" type="checkbox"/>	<input type="checkbox"/> MRI-based neuroimaging

Antibodies

Antibodies used

- 1) anti-DSRed (Takara/Clontech), catalog number: 632496, polyclonal, lot number: PK0495, dilution: 1/1000. This antibody has been validated to detect red fluorescent proteins in zebrafish (Ikenaga et al., 2011; PMID: 21452218).
- 2) anti-mCherry (Novus Biologicals), catalog number: NBP2-25158, polyclonal, lot number: 7670-3, dilution: 1/1000 This antibody has been validated to detect mCherry fluorescent proteins (Zhou et al, 2018; PMID: 30348769).
- 3) anti-GFP (Abcam), catalog number: ab13970, polyclonal, lot number: GR236651-23, dilution: 1/2000 This antibody has been validated to detect green fluorescent proteins in zebrafish. (Jiang D et al., 2019; PMID: 31371827).
- 4) anti-3A10 (DSHB), catalog number: AB_531874, monoclonal, dilution: 1/10. This antibody has been validated previously in zebrafish (Almeida RG et al., 2011; PMID: 21880787).
- 5) anti-Sox10 (GeneTex), catalog number: GTX128374, polyclonal, lot number: GTX128374, dilution: 1/2000. This antibody has been validated previously in zebrafish (Kroehne et al 2017; PMID: 28959189).
- 6) anti-MAP2 (Abcam), catalog number: ab11268, monoclonal, clone number: AP-20, lot number: GR3208593-2, dilution: 1/5000. This antibody has been validated previously in zebrafish (Lal et al, 2018; PMID: 29690872).
- 7) anti-acetylated tubulin (Sigma Aldrich), catalog number: T7451, monoclonal, clone number: 6-11B-1, lot number: 077M4751V, dilution: 1/2000. The antibody has been validated previously in zebrafish (Lepanto et al., 2016; PMID: 27053191).
- 8) anti-Gephyrin (Synaptic Systems), catalog number: 147 011, monoclonal, clone number: mAb7a, lot number: 1-63, Dilution: 1/500. This antibody has been validated previously in zebrafish (Yazulla S, Studholme KM, 2001; PMID: 12118162).
- 9) anti-rabbit AlexaFluor 555 (Invitrogen), catalog number: A-21428, polyclonal, lot number: 1903133, Dilution: 1/1000.
- 10) anti-mouse IgG1 Alexa Fluor 555 (Invitrogen), catalog number: A-21127, polyclonal, lot number: 2014177, Dilution: 1/1000. .
- 11) anti-chicken Alexa Fluor 488 (Invitrogen), catalog number: A-11039, polyclonal, lot number: 1899514, Dilution: 1/1000.
- 12) anti-mouse Alexa Fluor 633 (Invitrogen), catalog number: A-21052, polyclonal, lot number: 1848436, Dilution: 1/1000.
- 13) anti-mouse IgG2b Alexa Fluor 633 (Invitrogen), catalog number: A-21146, polyclonal, lot number: 1826341, Dilution: 1/1000
- 14) anti-rabbit Alexa Fluor 633 (Invitrogen), catalog number: A-21071, polyclonal, lot number: 1889315, Dilution: 1/1000
- 15) anti-chicken Alexa Fluor 555 (Invitrogen), catalog number: A-32932, polyclonal, lot number: UA2882077, Dilution: 1/1000

Validation

All primary antibodies have been validated in previous studies - please see the above section for an according reference for each antibody.

Animals and other organisms

Policy information about [studies involving animals](#); [ARRIVE guidelines](#) recommended for reporting animal research

Laboratory animals

Species: Danio Rerio, Strain: AB and nacre, Sex: female and male, Age: between 3dpf and 28 dpf

Wild animals

The study did not involve wild animals.

Field-collected samples

The study did not involve samples collected from the field.

Ethics oversight

All experiments carried out with zebrafish at protected stages have been approved by the government of Upper Bavaria (animal protocols AZ55.2-1-54-2532-199-2015 and AZ55.2-1-54-2532-200-2015 to T.C.).

Note that full information on the approval of the study protocol must also be provided in the manuscript.

Flow Cytometry

Plots

Confirm that:

- The axis labels state the marker and fluorochrome used (e.g. CD4-FITC).
- The axis scales are clearly visible. Include numbers along axes only for bottom left plot of group (a 'group' is an analysis of identical markers).
- All plots are contour plots with outliers or pseudocolor plots.
- A numerical value for number of cells or percentage (with statistics) is provided.

Methodology

Sample preparation

5 day old transgenic zebrafish with fluorescent labelled oligodendrocyte precursor cells (Tg[olig1:memEYFP]) were euthanised and de-yolked by repetitive pipetting embryos in de-yolking buffer (55mM NaCl, 1.2mM KCl, 1.25mM NaHCO₃) with a P1000 pipette tip. Following two wash steps in Danieau's buffer and centrifugation for 1' at 300 g, tissues were digested for 30 minutes at 37°C in a shaking incubator using the Papain Dissociation Kit (Worthington Biochemical Corporations) according to manufacturer's instructions.

Instrument

MoFlo XDP cell sorter (Beckman Coulter)

Software

Summit v5.2 software (for MoFlo XDP Beckmann Coulter) was used to collect data, and FlowJo v10 (Becton Dickinson)

Cell population abundance

The YFP+ cell population comprised 0.7% of all live cells, as determined by propidium iodide exclusion. Purity of the sample was determined by re-sorting the cells (prior to the final sorting into a 384 well plate), using Vybrant DyeCycle Ruby as a positive marker for live cells in the second sort. This allowed for a second exclusion of any non-YFP+ cells.

Gating strategy

The gating strategy was set up using wild type fish lacking YFP+ cells, before sorting YFP+ cells. The sorting strategy for the YFP+ cells is as follows: on the first sort, large/small debris is excluded by drawing a gate around cells with 1.0-3.0K forward and side scatter. By looking at forward scatter vs width, we could include only single cells and exclude large 'doublets'. Propidium iodide staining was used to exclude dead cells (defined by fluorescent signal >50). Then, the cells with high YFP+ expression were sorted (fluorescent signal >300). On the second sort into a 384 well plate, the same same sorting strategy was performed, apart from Vybrant DyeCycle Ruby as a positive marker for live cells (fluorescent signal >30). YFP+ cells were sorted from these populations (again, defined as fluorescent signal >300).

- Tick this box to confirm that a figure exemplifying the gating strategy is provided in the Supplementary Information.